Perovskite solar cells: film formation and properties

Tze-Bin Song,[ab] Qi Chen,[ab] Huanping Zhou,*[ab] Chengyang Jiang,[ab] Hsin-Hua Wang,[ab] Yang (Michael) Yang,[ab] Yongsheng Liu,[ab] Jingbi You[ab] and Yang Yang*[ab]

Perovskite solar cells have received considerable attention in recent years as a promising material capable of developing high performance photovoltaic devices at a low cost. Their high absorption coefficient, tunable band gap, low temperature processing and abundant elemental constituents provide numerous advantages over most thin film absorber materials. In this review, we discuss the current status of $CH_3NH_3PbX_3$ (X = I, Br, Cl) based photovoltaic devices and provide a comprehensive review of $CH_3NH_3PbX_3$ device structures, film properties, fabrication methods, and photovoltaic performance. We emphasize the importance of perovskite film formation and properties in achieving highly efficient photovoltaic devices. The flexibility and simplicity of perovskite fabrication methods allow use of mesoporous and planar device architectures. A variety of processing techniques are currently employed to form the highest quality $CH_3NH_3PbX_3$ films that include precursor modifications, thermal annealing and post-deposition treatments. Here we outline and discuss the resulting material qualities and device performances. Suggestions regarding needed improvements and future research directions are provided based on the current field of available literature.

1. Introduction

The recent advent of organometallic lead halide perovskite solar cells has produced some of the most rapid growth in cell performance of any material in photovoltaic history.[1–3] The unique properties of these absorber layers provide a number of advantages in optoelectronic applications that in many ways originate from the nature of the perovskite lattice.[4–6] The exclusive use of widely available elements and the capacity for film deposition through either solution or vacuum-based methods is an indication of the tremendous potential of these compounds to completely redefine the way that materials are designed and chosen for electronic device applications. The

[a]Department of Materials Science and Engineering, University of California Los Angeles, Los Angeles, California 90095, USA. E-mail: happyzhou@ucla.edu; yangy@ucla.edu

[b]California NanoSystems Institute, University of California Los Angeles, Los Angeles, CA 90025, USA

Tze-Bin Song is a Ph.D candidate at the University of California Los Angeles (UCLA), in Materials Science and Engineering under the supervision of Prof. Yang Yang. He received his B.S. degree from National Tsing-Hua University, Taiwan, in 2007 and M.S. degree from University of Florida in 2010, both in Materials Science and Engineering. His research interests include development of thin film solar cells, transparent electrodes and material/device characterizations. During his Ph.D. studies, he had an internship in International Business Machines, T. J. Watson, NY, where he participated in developing the advanced integration technique.

Dr. Qi Chen received his Ph.D degree in Materials Science and Engineering from University of California at Los Angeles (UCLA) in the year 2012. Now, he is working as a postdoc fellow in California Nanosystem Institute (CNSI) of UCLA. His research focuses on hybrid materials and polymer blends for various applications, such as photovoltaics, sensors, detectors, etc.

scope of this review is to summarize the notable achievements in hybrid perovskite film formation: (1) film formation methods, (2) techniques to tune film properties, and (3) cell architecture, performance, and optimization.

Perovskite materials follow the general formula ABX_3 and adopt the same crystal structure as calcium titanate. In this arrangement, the 'A' and 'B' cations coordinate with 12 and 6 'X' anions, forming cuboctahedral and octahedral geometries, respectively (shown in Fig. 1).[7] The tendency of a compound toward perovskite formation can be estimated using the Goldschmidt tolerance factor,[8] although determining the chemical and thermal stability of the resulting structure invariably requires more detailed analysis. The perovskite material family exhibits a wide range of electronic behavior including piezoelectric, thermoelectric, semiconducting, and superconducting properties depending on the specifics of the measured material.[9–12] In the early 1990s, Mitzi and coworkers made an extensive investigation into the optoelectronic properties of organometallic halide perovskites, where the 'A' sites are occupied by organic cations, the 'B' sites are occupied by group
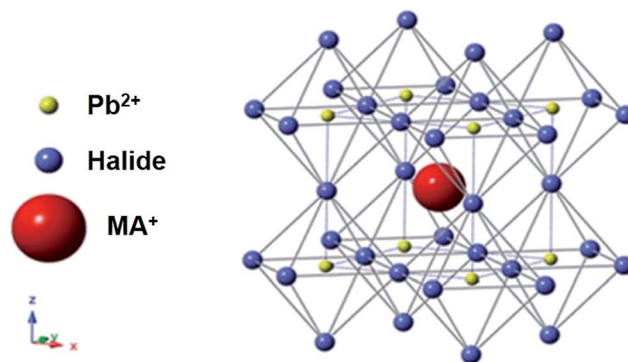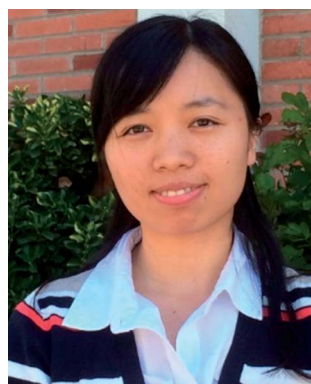

Fig. 1 Crystal lattice of the methylammonium lead halide (CH_3NH_3-PbX_3) perovskite structure. Adapted with permission from ref. (7). Copyright 2013 Nature Publishing Group.

IV cations (Sn, Pb), and the 'X' sites are occupied by group VII anions (Cl, Br, I).[13–16]

Lead halide perovskite solar cells are rapidly approaching 20% power conversion efficiency (PCE) after only 5 years of

Dr. Huanping Zhou received her Ph.D degree in Inorganic Chemistry from Peking University in the year 2010. Now, she is working as a postdoc fellow in Prof. Yang Yang's lab in UCLA. Her research focuses on nanomaterials, thin films, optoelectronics, etc.

Yang (Michael) Yang received a B.E. in Electrical Engineering from Zhejiang University, China in 2009. He was a research intern between 2009 and 2010 at Institute of Chemistry, Chinese Academy of Sciences (ICCAS), under the supervision of Prof. Yongfang Li. He is now a Ph.D candidate in Prof. Yang Yang's group, in the Department of Materials Science and Engineering at UCLA. His research interests include organic and organic–inorganic hybrid optoelectronic devices and their spectroscopic study.

Dr Chengyang Jiang got his B.S. in chemistry from Peking University in China, and his Ph.D in chemistry from the University of Chicago under the supervision of Dmitri V. Talapin. His Ph.D thesis title is "Design and Mechanistic Study of New Precursors for Solution-Processed Semiconductors". In 2014, he joined Prof. Yang Yang's group at Department of Materials Science and Engineering at UCLA as a postdoctoral scholar, focusing on the solid-state chemistry of high-performance thin film solar cells, especially $Cu_2ZnSn(S,Se)_4$ (CZTS). He has broad research interests at the interface of materials chemistry and renewable energy.
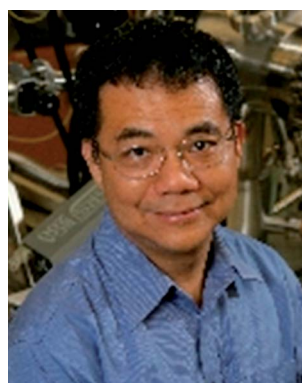
Yang Yang received his M.S. and Ph.D in Physics and Applied Physics from the University of Massachusetts, Lowell in 1988 and 1992, respectively. Before he joined UCLA in 1997, he served as research staff in UNIAX (now DuPont Display) from 1992 to 1996. Yang is now the Carol and Lawrence E. Tannas Jr Endowed Chair Professor of Materials Science at UCLA. He is also a Fellow of MRS, SPIE, RSC and the Electromagnetic (EM) Academy. He is an expert in the fields of organic, inorganic and organic–inorganic hybrid electronics and the development and fabrication of related devices, such as photovoltaic cells, LEDs, transistors and memory devices.

concerted development, an achievement that required decades of effort for conventional materials.[2,17–19] The most successful perovskite materials thus far are variations on the compound $CH_3NH_3PbX_3$ (X = Cl, Br, I), which exhibits the most attractive properties of ideal PV absorbers: (1) strong optical absorption due to s–p anti-bonding coupling; (2) high electron and hole mobilities and diffusion lengths; (3) superior structural defect tolerance and shallow point defects; and (4) low surface recombination velocity and benign grain boundary effects.[20–23]

The hybrid organic–inorganic nature of halide perovskites has allowed this class of materials to capitalize on the previous development of Dye-Sensitized Solar Cells (DSSCs), organic photovoltaics, and other thin film material systems.[24–27] In a typical cell architecture, a perovskite absorber layer with a thickness of several hundred nanometers is sandwiched between an electron and hole transport layer (ETL and HTL).[28–30] When the device is illuminated, carriers are created in the absorber, extracted by the ETL and HTL and collected at the appropriate electrodes. The work required for establishing a rational guide for fabricating high quality absorber layers is still underway, and is made more difficult by the unique characteristics of perovskite films in the context of their materials chemistry and physics. Additional efforts related to connecting the structure and composition of perovskite absorbers to their electronic properties and device performance are particularly valuable in enhancing our understanding of how to process and deposit films formed from this material family.

2. Film formation

To date, various processing techniques have been documented to fabricate hybrid perovskite films, mainly one-step or two-step sequential deposition methods based on solution processing, vacuum deposition, or vapor assisted solution processing.[31–33] It has also been suggested that the optoelectronic properties of perovskite films are closely related to the processing conditions, such as the starting material ratio and the atmospheric conditions during film growth, which lead to a substantial difference in the film quality and device performance.[34,35] The kinetic and thermodynamic parameters that govern lattice formation have been investigated either by tuning the annealing temperature, time, and ramping rate, or by employing different solvents or additives.

One of the key reasons for the rapid increase in power conversion efficiency (PCE) of perovskite devices is a growing understanding of film formation mechanisms and the continuous improvement in processing approaches for perovskite materials. Hybrid perovskite materials form with crystallinity, even when processed at low temperatures, and the formation of the final perovskite phase benefits from the relatively high reaction rates between the organic and inorganic species. These advantages substantially expand the choices of available processing methods such as thermal evaporation and solution processing, and facilitate the adoption of new and varied device architectures.

Unique from most inorganic and organic materials, forming high quality perovskite films is complicated by the distinctly different physical and chemical characteristics of the organic and inorganic components.[14,22,36–38] For example, organic materials tend to be soluble in different solvents than those appropriate for processing the inorganic framework, which results in poor film quality when using solution deposition techniques. For those cases where both materials are soluble, solution techniques must be judiciously controlled because of adverse substrate wetting characteristics and the fast intercalation reaction. With regard to vacuum deposition techniques, poor control of the heating of the two reactant species and substrate temperature typically results in the decomposition or dissociation of the organic component, or non-ideal stoichiometry in the final film.

One step and sequential deposition (either in solution or vacuum) techniques have been demonstrated in perovskite solar cells based on two typical architectures: mesoporous scaffold and planar heterojunction configuration (schematic diagram shown in Fig. 2).[39] One-step processing is based on the co-deposition of both the organic and inorganic components either through solution processing or thermal evaporation. In solution processing, a mixture of MX_2 (M = Pb, Sn; X = Cl, Br, I) and AX (A = methylammonium, MA; formamidinium, FA) is dissolved in an organic solvent and deposited directly to form a film and followed by thermal annealing to produce the final perovskite phase.[40] Meanwhile, thermal evaporation employs dual sources for MX_2 and AX with different heating temperatures to form the perovskite film.[32] Sequential deposition is namely depositing an MX_2 (M = Pb, Sn; X = Cl, Br, I) layer such as PbI_2 and an AX (A = MA, FA) such as methylammonium iodide (MAI) sequentially followed by heat treatment to form the completed perovskite film.[41–43]

Typically, the deposition of MX_2 is achieved using spin-coating, while AX can be introduced by (1) spin-coating the AX solution on top of the MX_2 layer, (2) immersing the MX_2 layer in the AX solution to induce a solid–liquid reaction, or (3) exposing the MX_2 layer to AX vapor at elevated temperatures.[33,44,45] Also, two-step sequential deposition can be carried out in thermal evaporation, by sequentially depositing the inorganic and organic components. The schematic diagrams of different deposition methods are shown in Fig. 3.

In this section, two major perovskite device structures with corresponding deposition methods and the unique perovskite film properties based on the phase formation, defect states and electrical and optical properties are discussed in the following subsections.
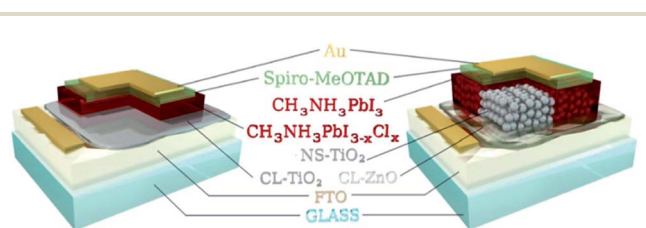

Fig. 2 Perovskite solar cell device structure: (Left) planar structure, (Right) mesoporous scaffold. Adapted with permission from ref. (39). Copyright 2014 American Chemical Society.
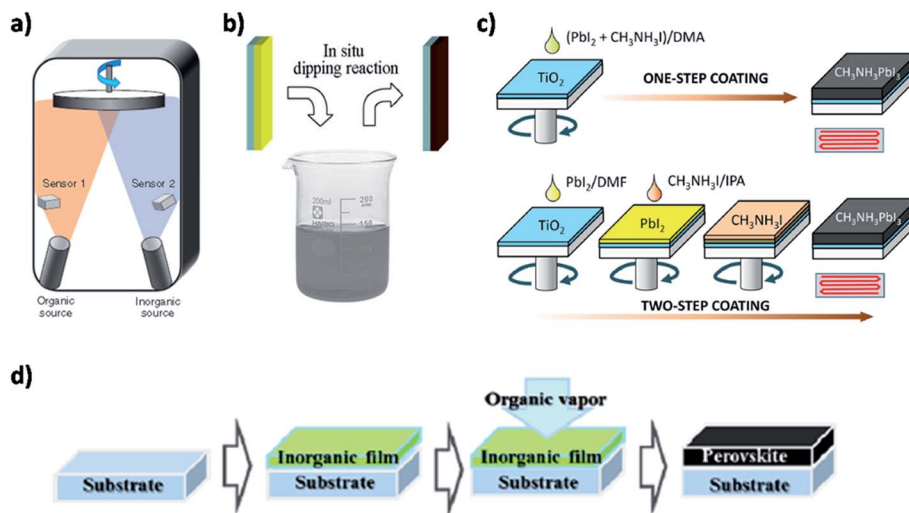
Fig. 3 The preparation of MAPbI$_{3-x}$Cl$_X$ film from different deposition methods: (a) Dual source coevaporation using PbCl$_2$ and MAI source. (b) Sequential deposition by dipping the PbI$_2$ film into MAI solution. (c) One-step solution process based on the mixture of PbI$_2$ and MAI, and sequential coating of PbI$_2$ and MAI (d) Vapor-assisted solution process using the MAI organic vapor to react with the PbI$_2$ film. Adapted with permission from ref. (32, 33, 44 and 45). Copyright 2013 Nature Publishing Group, 2014 American Institution of Physics, 2014 American Chemical Society.

2.1 Mesoporous structures

The first use of hybrid perovskite absorbers in photovoltaic cells is based on the typical structure of a dye-sensitized solar cell, where the perovskite absorber is self-assembled within the gaps of a porous TiO$_2$ layer formed by sintering nanoparticles.[46–48] The typical configuration of this type of perovskite-based solar cell is FTO/dense TiO$_2$/mesoporous TiO$_2$/perovskite/[2,2',7,7'-tetrakis-(N,N-di-4-ethoxyphenylamino)-9,9'-spirobifluorene](Spiro-OMe-TAD)/electrode, as shown in Fig. 4. In this structure, perovskite materials are deposited onto mesoporous TiO$_2$, which is used to facilitate electron transport between the perovskite absorber and the FTO electrode.[49] A subsequent work demonstrated the replacement of relatively conductive porous TiO$_2$ with an insulating porous Al$_2$O$_3$ layer.[50] The successful use of an insulating Al$_2$O$_3$ scaffold indicated that perovskites have a broader potential than just being used as sensitizers, as they are able to transport both electrons and holes between cell terminals.

A typical fabrication procedure for mesoporous scaffold-based perovskite solar cells is as follows. Fluorine-doped Tin Oxide (FTO) substrates are used with a compact TiO$_2$ blocking layer and a mesoporous oxide layer that have each undergone high temperature sintering steps (500 °C). Afterwards, the perovskite absorber layer is deposited. For one-step processing, pure iodine-based MAPbI$_3$ is generally deposited from a mixture of PbI$_2$ and MAI in N,N-Dimethylformamide (DMF), γ-butyrolactone (GBL), or a similar solvent system. One-step processing has also achieved success in mixed halide material systems, where mixed PbCl$_2$ and MAI at a 1 : 3 molar ratio in DMF were deposited onto an insulating Al$_2$O$_3$ mesostructured scaffold.[50] Finally, Spiro-OMeTAD and the metal electrode were deposited by spin-coating and thermal evaporation respectively to complete the device. An inverted p–i–n mesoporous structure based on FTO/compact NiO$_X$/nanocrystal NiO/perovskite/PCBM/electrode can also be achieved with a similar fabrication process.[51]

It is worth noting that successful pore-filling in mesoporous structures is important in order to prevent leakage through the device, which has been a problem for thick mesoporous
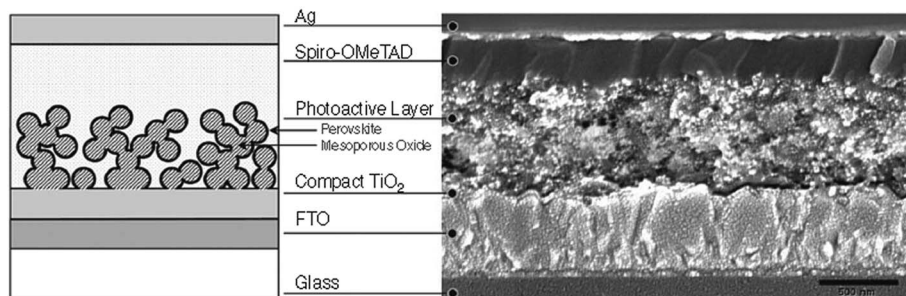

Fig. 4 (Left) The schematic diagram and (Right) cross-section SEM of the mesoporous structured perovskite solar cell device. Adapted with permission from ref. (50). Copyright 2013 American Association for the Advancement of Science.

structures.[52] Therefore, the placement of a thin perovskite capping layer on top of mesoporous structures is often used to enhance light absorption and prevent possible shunting pathways.[53] This is usually achieved by increasing the concentration of the precursor solution, causing excess material to build up on top of the porous scaffold layer.

A number of crucial parameters are involved in this type of deposition procedure, which affects the grain size, crystallinity, and surface coverage of the resulting films. For example, solvent engineering techniques, where a small amount of additional drop is added during spin-casting, has recently been shown to remove the solvent originating from the perovskite solution while greatly enhancing the grain size, coverage, and uniformity of the capping layer on the mesoporous structure.[54] More detailed discussion of controlling film formation parameters will be addressed in the next section.

In two-step sequential processing, PbI_2 is first deposited onto a mesoporous substrate and the perovskite film is formed either by dipping the substrate in a MAI solution or spin-casting the MAI solution onto the PbI_2 film while using a solvent that does not dissolve PbI_2.[41,55] The resulting perovskite film has been shown to improve the coverage of the capping layer, compared to a one-step process, by retaining the morphology of the original PbI_2 film, which is quite uniform after spin-casting. Incorporating a certain amount of $PbCl_2$ in PbI_2 in the first step offers an additional opportunity to optimize morphology control.[56,57] The grain size of the deposited perovskite film in mesoporous structures is found to be confined by the pore size of the mesoporous scaffold.[55,58] Though perovskite absorbers are known to have relatively benign grain boundaries, large grains are still desirable for reducing possible recombination paths and improving carrier transport.[20,59,60]

The use of mesoporous structures as a scaffold to fabricate perovskite solar cells has led to an increase in device performance from 3.8% to over 17% PCE in the period of a few years.[1,35,54,61] As the mesoporous structure does not rely on long carrier diffusion length, it is also able to provide a forgiving platform within which to investigate the new perovskite materials. While the use of a mesoporous scaffold requires a comparatively complex device architecture and fabrication process in which many problems can arise, it has consistently delivered high efficiencies that make its use fully worthwhile for laboratory scale investigations.

2.2 Planar structure

In a planar junction perovskite solar cell, a several hundred nanometer thick absorber layer, is sandwiched between ETL and HTL without a mesoporous scaffold. As the hybrid perovskite exhibits ambipolar carrier transport and long carrier lifetimes, solar cells with planar configurations can deliver efficiency values of over 15% despite being under development for an even shorter period than their mesoporous counterparts.[6,50] This architecture offers the advantages of a simplified device configuration and fabrication procedure, and so has rapidly acquired the interest of the thin film research community. Planar structures are most commonly illuminated from the

n-type side, resulting in the structure glass/TCO/ETL/perovskite/HTL/metal, or p-type side, resulting in the inverted structure glass/TCO/HTL/perovskite/ETL/metal which functions in a superstrate configuration.[62–64]

The earliest attempts to fabricate planar perovskite solar cells used single step deposition to deposit the perovskite absorber layer. The lack of an existing porous scaffold has a dramatic effect on the coating and growth of the perovskite material, and so additional optimization is often necessary when converting a deposition method from mesoporous to planar structures. For dual-source vacuum deposition, the final films are typically very uniform with excellent surface coverage, as seen in the SEM images in Fig. 5(a).[32] Compared to the mesoporous scaffold, thermal evaporation can be more efficiently applied in a planar configuration, without worrying about the difficulty of perovskite precursors penetrating into the nanoporous scaffolds.

One-step solution processing has also been demonstrated in the planar configuration by mixing MAI and $PbCl_2$ in DMF to form $MAPbI_{3-X}Cl_X$.[65,66] Unlike mesoporous structures, forming a continuous perovskite film is critically important for planar structures, as the presence of pinholes may cause a severe leakage current. For example, the $MAPbI_3$ is prone to forming fiber-shaped crystals in planar films, resulting in poor device performance. Numerous studies have been designed to advance our understanding of film formation with respect to a variety of processing parameters, e.g. thermal annealing conditions, stoichiometry of organic and inorganic species, substrates, additives, solvent engineering and atmospheres, each of which are discussed in the following sections.

In addition to one-step deposition, the perovskite film can be prepared using sequential deposition procedures. Adopted from the mesoporous structure, Liu et al. demonstrated a high
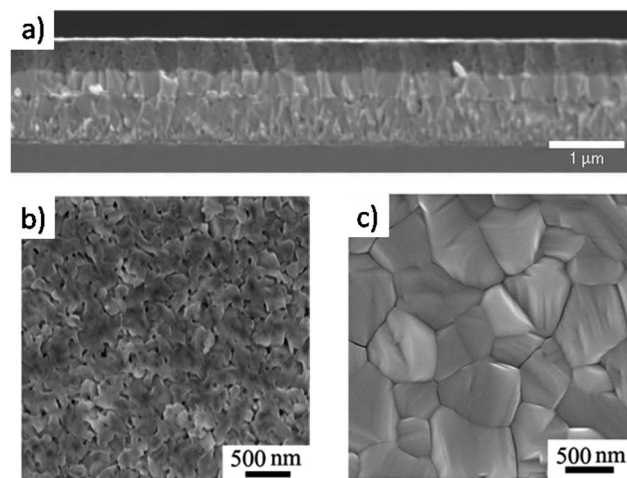

Fig. 5 (a) Cross-section SEM images of the perovskite film prepared by dual source coevaporation. The perovskite layer with homogeneous and flat boundaries can be distinguished clearly. (b) The as-deposited PbI_2 layer by solution process and (c) the perovskite film with micrometer grain size, obtained by the vapor assisted solution process. Adapted with permission from ref. (32 and 33). Copyright 2013 Nature Publishing Group, 2014 American Chemical Society.
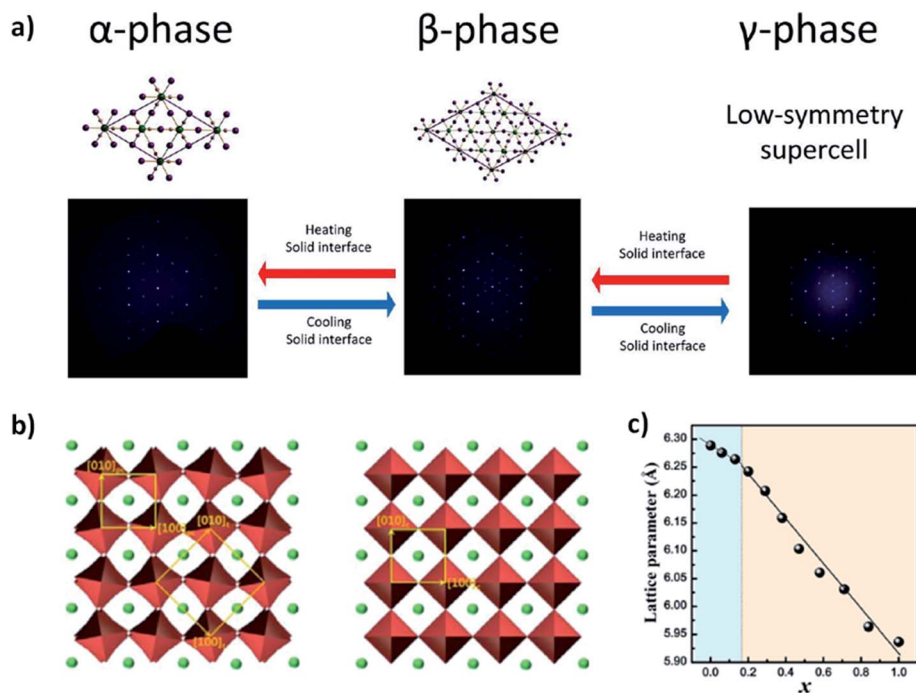
Fig. 6   (a) Graphical scheme of observed phase transitions of MA(Pb,Sn)X$_3$ perovskite materials. Precession images are drawn at [006] view. (b) The structure transformation from the Br incorporation in MAPbI$_3$ and (c) the lattice contact change with different amounts of Br incorporation. Adapted with permission from ref. (68 and 73). Copyright 2014 American Chemical Society.
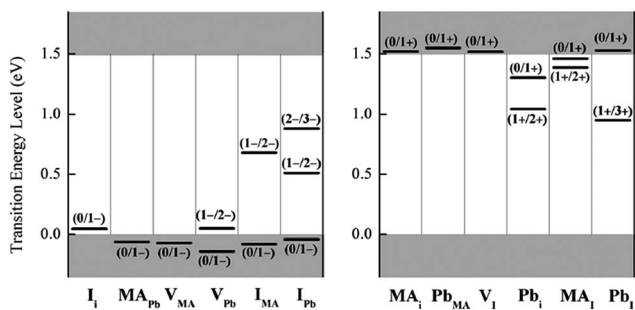

Fig. 7   Defect diagram of MAPbI$_3$ perovskite from DFT calculation: (Left) the intrinsic acceptors and (Right) intrinsic donors. Adapted with permission from ref. 80. 2014 American Institution of Physics.

performance (15.7%) planar cell using sequential deposition processing, where the deposited PbI$_2$ film was soaked in a MAI solution to form the final perovskite phase.[67] This two-step process can effectively reduce the chemical reaction between the perovskite materials and the underlying electron transport layer, as MAI dissolved in DMF was suspected to provide an acidic environment which could quickly etch the ZnO during subsequent annealing steps. The development of sequential deposition methods has provided a variety of ETL options, while allowing for perovskite films to be prepared effectively at room temperature.

In addition, Chen *et al.* developed a vapor assisted solution processing (VASP) method that used the reaction between MAI vapor and pre-deposited PbI$_2$ to form the completed perovskite film.[33] The resulting MAPbI$_3$ exhibits excellent film quality, *e.g.*

full surface coverage, large grain size on the micrometer level, and improved film conformity. The phase and film evolution from PbI$_2$ to MAPbI$_3$ was recorded using XRD and SEM characterization as shown in Fig. 5(b and c), where the MAI reacted with PbI$_2$ to form MAPbI$_3$ from the PbI$_2$ surface and into the film to achieve a complete transformation. Xiao *et al.* developed a two-step solution coating method that used two separate depositions of PbI$_2$ and MAI followed by an annealing step to prepare MAPbI$_3$.[41] High performance perovskite devices are demonstrated by controlling the preparation conditions, *e.g.* the concentration of PbI$_2$ and MAI, coating spin-speed, and the subsequent annealing temperature/time based on this method.

One of the useful aspects of sequential procedures is their reliance on PbI$_2$ precursor films as a template to form the eventual perovskite layer. This avoids one of the major problems associated with one-step solution processing, in which fiber-shaped crystals often form as the MAPbI$_3$ phase grows directly from solution. Due to its simplified fabrication and ease of deposition, the planar architecture provides great promise in future applications, including high performance flexible and portable devices.

2.3   Phase formation

The perovskite phase with a general formulation ABX$_3$ are structures containing 'A' cations and interconnected [BX$_6$] octahedra. Depending on the relative sizes of the cation and the octahedron, the perovskite phase can be three-dimensional (3D), two-dimensional (2D) or even one-dimensional (1D) in crystal structure.[68] Within the scope of this article, we will only
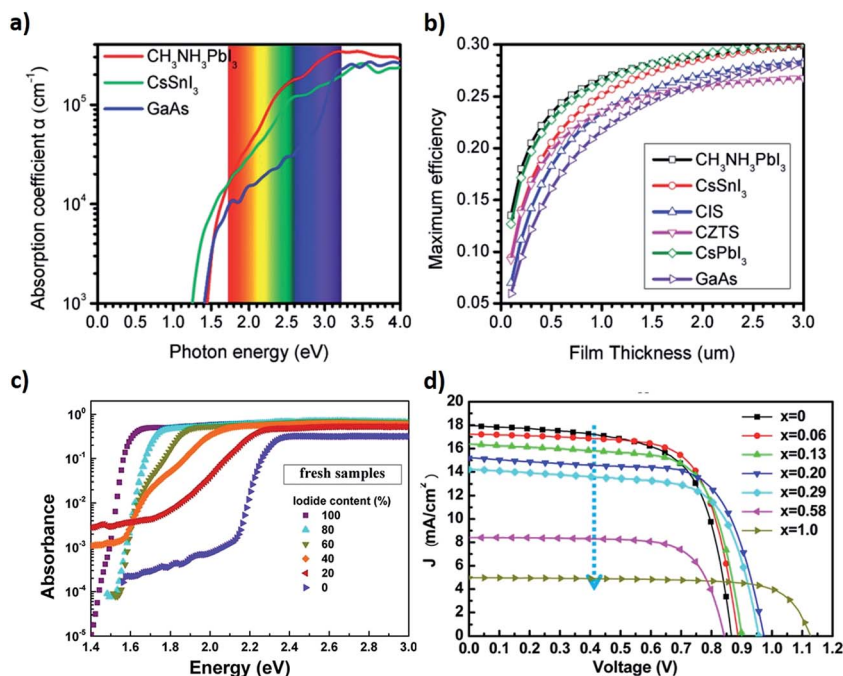
Fig. 8 (a) The calculated absorption coefficient of MAPbI$_3$, CsSnI$_3$ and GaAs materials, respectively. (b) The calculated maximum PCE of different photovoltaic absorber materials at different film thicknesses. (c) Absorbance spectra of different ratios of Br in MAPbI$_{3-x}$Br$_x$ materials. (d) $J–V$ curves of different Br ratios in MAPb(I$_{1-x}$Br$_x$)$_3$ devices. Adapted with permission from ref. (20, 73 and 84). Copyright 2014 Wiley, 2014 American Chemical Society.

focus on three-dimensional (3D) organometal halide perovskite phases with demonstrated optoelectronic applications. Within the crystal lattice, 'A' represents a protonated amino group MA$^+$ or FA$^+$, 'B' represents Pb^{2+} or Sn^{2+}, and 'X' represents I$^-$, Br$^-$, or Cl$^-$.

With the rare exception of using single-source thermal ablation to generate the perovskite phase, the formation of perovskite structures usually follows the overall formula AX + BX$_2$ → ABX$_3$.[69] Using the following reaction as a typical example:

$$PbI_2 + MAI \rightarrow MAPbI_3$$

It has been observed that the reaction kinetics of perovskite phase formation are impressively fast.[67] During the transformation into the perovskite lattice, spaces are formed between the layered [PbI$_6$] octahedral that share facets in PbI$_2$ to create [PbI$_6$] octahedra that share only vertices in MAPbI$_3$. Solvation of PbI$_2$ is another important parameter that affects the intermediate reaction stage. Since it has been demonstrated that the soft Pb(II) can easily coordinate with a variety of small molecules (such as ethanolamine[70] or dimethyl sulfoxide (DMSO)[71]), after which the original facet-sharing [PbI$_6$] octahedra are partially disintegrated and small ligands are inserted, it is therefore logical to conclude that during the dissolution of PbI$_2$, solvent molecules partially replace iodine to ligate with lead, thus facilitating the subsequent reaction forming the perovskite phase. Such a concept has recently been further

taken advantage of by using mixed solvents to rationally control the reaction kinetics for optimized film formation.[54]

Besides the kinetics of phase formation, another interesting topic is the formation of mixed-cation, mixed-group IV metal, and mixed-halide perovskite phases, allowing for the fine tuning of the optical and electronic properties of the final material. Among them, the most extensively studied combination is mixed halides, which was first demonstrated as a sensitizer in 2012.[50] Although such a phase was initially denoted as MAPbI$_2$Cl, it was later discovered that the doping level of chlorine into iodine perovskite is actually limited to below 4%, irrespective of the combination of precursors used (MAI + PbCl$_2$ or MACl + PbI$_2$).[72] Such phenomenon is due to the large discrepancy of ionic size between Cl$^-$ and I$^-$, as opposed to the Br$^-$/I$^-$ perovskite whose ratio between two halides can be freely tuned from 0 to 1.[73,74]

A perovskite phase with mixed-group IV metals has recently been synthesized using MAI and a mixture of PbI$_2$ and SnI$_2$.[75] Lead and tin were determined to be randomly distributed in the [MX$_6$] octahedra and the percentage of tin content in the perovskite could be tuned from 0 to 1, but the resulting shift in band structure does not follow the normal Vegard's law due to the changed origin of conduction and valence band edges with various Pb/Sn ratios. Moreover, perovskite phases with mixed organic cations have also been reported. Typically, the mixture of MAI and FAI can be used to prepare such a mixed-cation phase, which shows enhanced harvesting of red photons and longer carrier lifetime.[56] Furthermore, the templating effect of a secondary cation on the formation of preferentially oriented

perovskite phases has also been explored.[76,77] Through doping MAI with 5-ammoniumvaleric acid (5-AVA) iodide, the resultant perovskite phase preferentially grows along the c-axis, thus reducing the apparent concentration of structural defects.

MAPbX$_3$-based perovskites have been found to exhibit multiple phases as a function of temperature and composition. These different phases possess dramatically different electrical/optical properties as well as stability. Stoumpos et al. showed that MAPbI$_3$ exhibited an α-phase, δ-phase, and γ-phase with transition temperatures of 400 K, 333 K, and 180 K, respectively as shown in Fig. 6(a).[68] In general, the δ-phase MAPbI$_3$ is used as the solar cell absorber because of its thermodynamically stable nature at room temperature and its increased absorption coefficient (>26 mm^{-1}) and conductivity, in contrast to the α-phase. However, a possible phase transition from δ-phase to α-phase may occur under continuous 1 sun illumination, which requires more detailed examination.

Phase transformation can occur in mixed halide systems. Noh et al. used a mixed halide MAPbI$_{3-X}$Br$_X$ ($0 \leq X \leq 3$) for band-gap tuning and observed that the crystal structure transformed from the tetragonal phase to a cubic phase when the percentage of Br present passed a threshold of approximately $X \approx 0.5$, as shown in Fig. 6(b).[73] This phase transition has been presumed to explain the improved stability of MAPbI$_{3-X}$Br$_X$ materials in the air and humidity test, making it an interesting addition to our understanding of the specifics of the perovskite lattice.

2.4 Defect energy

One merit of the organic–inorganic hybrid perovskite semiconductor is the unusually long carrier lifetime despite its direct band gap and polycrystalline nature. Moreover, perovskite semiconductors also show very efficient photoluminescence quantum yield and even optically pumped lasing effects.[78,79] The high emissive quantum yield and long carrier lifetime indicates that the non-radiative recombination channel is strongly inhibited, which is an excellent sign of its applicability in optoelectronic device fabrication.

Yin et al. shed some light on the unusual defect physics through density-functional calculations on the perovskite lattice.[20,80] The organic–inorganic hybrid perovskite material is composed of three ion types: positively charged methylammonium (MA$^+$) and lead, and negatively charged iodide. Interestingly, the defects with the lowest formation energies are Pb vacancies and interstitial MA$^+$. However, both defects only create shallow charge-carrier states near the perovskite band edges as shown in Fig. 7.

Such shallow defects do not serve as severe non-radiative recombination centers the way that deep defects with energy levels near the middle of the bandgap do. The lack of deep trap states within the band gap of the perovskite band structure to some extent explains its long carrier lifetime, as well as its superior electronic device performance. In addition, the Pb vacancy is an electron acceptor while the interstitial MA$^+$ is an electron donor, and the presence of these two defects is

sensitive to preparation methods. In other words, whether the perovskite film is p-type or n-type may be dependent on how it is prepared.

However, it should be noted that all the above theoretical studies indicate that the grain boundary does not introduce deep defect states, but the interface states between the perovskite and HTL or ETL, e.g. TiO$_2$, Spiro-OMeTAD, PCBM, etc., might still be detrimental, as they can easily serve as sites for interfacial recombination. Further investigation on the interface states of perovskite materials when operating in a real solar cell would be highly beneficial in beginning to resolve this issue.

2.5 Optical and electrical properties

MAPbX$_3$-based materials exhibit attractive optical and electrical properties. The p–p transition and direct bandgap result in a higher absorption coefficient (α) as compared to CsSnI$_3$ and GaAs, as shown in Fig. 8(a). The high α value (>10^5 cm^{-1}) provides a great potential to fully utilize the photon energy larger than the bandgap and delivers high J_{SC} from thin film (~300 nm) devices.[20] Compared with CIGS, GaAs, and Si-based solar materials, MAPbX$_3$-based materials could achieve highest PCE for a given thickness as shown in Fig. 8(b). Moreover, the high V_{OC} value (~1.15 V) was achieved on MAPbI$_3$ devices relative to its optical bandgap (~1.5 eV). The small V_{OC} deficit of the MAPbI$_3$ device can be attributed to the less deep defect states and efficient interface contacts. From the optical measurement, the sharp absorption edge measured from photothermal deflection spectroscopy and Fourier-transform photocurrent spectroscopy on the MAPbI$_3$ material shows the well-ordered microstructure and negligible deep states. De Wolf et al., observed the Urbach energy of 15 meV in MAPbI$_3$ which is closer to high quality GaAs materials.[81] The results indicated the lower possibility of non-radiative recombination that can occur in the MAPbI$_3$ materials and directly supported the shallow defect properties from the theoretical calculation discussed in the previous section.

With regard to the electric property, perovskite materials has proven to exhibit ambipolar carrier transport behavior and long carrier lifetime. The effect was firstly noticed by using insulating Al$_2$O$_3$ structure as the scaffold, while the electrons and holes can be collected efficiently.[50] Through electron beam induced current (EBIC) measurement on the perovskite device, the carriers can be collected on both electrodes when the electron beam focused on either one side of the perovskite layer, which further supports the ambipolar effect in MAPbX$_3$-based materials.[82] More than 1 μm diffusion length and more than hundreds of nanoseconds carrier lifetime were characterized.[83] This indicated the relatively prohibited non-radiation recombination process and the suppressed defect/trap associated recombination of free carriers during transporting. These electrical properties allow the perovskite materials to serve as an efficient transporting layer while being an excellent absorber.

Furthermore, mixed halides with tunable bandgap, such as MAPbI$_{3-X}$Br$_X$ have also been intensively studied. Noh et al.

tuned the bandgap by incorporating different ratios of I and Br, where the optical bandgap relationship is fitted as follows:[73]

$$E_g(x) = 1.57 + 0.39x + 0.33x^2 \quad (x \text{ is the ratio of } Br/(Br + I))$$

A larger Urbach energy in the mixed halide $MAPbI_{3-x}Br_x$ was noticed by Sadhanala *et al.*, although there is no defect analysis at the current stage.[84] Introducing Br content in $MAPbI_{3-x}Br_x$ changes the tail states in the optical spectrum and a rather high Urbach energy (90 meV) was found for $MAPbI_{0.6}Br_{2.4}$ as shown in Fig. 8(c). The increase of Urbach energy indicates a more disordered structure and increased defect state in the materials, which might be caused by the disorientation of Br species or non-uniform distribution of I/Br element during the film formation.

The different electrical properties of the $MAPbI_{3-x}Br_x$ perovskite materials are investigated based on the corresponding device performance. It is worth noticing that the V_{OC} value of the devices does not follow the trend of the optical bandgap change as shown in Fig. 8(d).[73] A rather higher Br content in $MAPbI_{3-x}Br_x$ leads to an increased bandgap of materials, but a decreased V_{OC} in the devices. Photo-induced phase segregation while $X > 0.6$ has been observed by Hoke *et al.*, where two crystalline phases and a low energy PL peak occurred under 1-sun illumination. These two phases were suspected to be iodide-rich domain and bromide-rich domain, resulting in a new red-shifted PL peak. The PL results indicated a reduction in the electronic bandgap and quasi-Fermi level splitting which reduced their achievable V_{OC}.[85] Suarez *et al.* further examined a system with three halides (Cl, Br and I), and found the recombination rate can be reduced by simultaneously incorporating Cl and Br to $MAPbI_3$.[86] These optical and electrical characterizations indicated that the Cl species may help to evenly mix I and Br species during the film formation to further reduce the recombination and improve the device performance.

3. Film quality

As indicated in the previous section, perovskite materials exhibit a wide range of film properties *e.g.* grain size, morphology, crystallinity, surface coverage, *etc.*, based on various processing approaches. Pioneering work has also suggested that perovskite films exhibit composition/structure dependent properties by adjusting the metal halide framework and the intercalated organic species. Thus, it is essential to achieve fine control over the reaction between the inorganic and organic species, resulting in perovskites with desirable properties and device performance. Various process parameters including the stoichiometry, thermal treatment, solvent engineering, additives, and environmental control, which were incorporated to improve the perovskite film qualities will be discussed in the this section.

3.1 Stoichiometry

The stoichiometry, particularly the ratio of the organic and inorganic component, largely affects the resulting $MAPbI_{3-x}Cl_x$ film quality in terms of film conformity and carrier behavior.

Generally, a solution of PbX_2 and MAX with a stoichiometry of 1 : 1 is used as the precursor to form a pure perovskite phase. For example, the MAI and PbI_2 (1 : 1 mole ratio) were dissolved in GBL and deposited on a mesoporous structure to form a $MAPbX_3$ film.[87,88] However, when starting from the mixture of $PbCl_2$ and MAI solution, a non-stoichometric mole ratio of 1 : 3 is demonstrated to be optimum for the formation of $MAPbI_{3-x}Cl_x$ films.[89,90]

This kind of stoichiometry (PbI_2 : MAI = 1 : 1, or $PbCl_2$: MAI = 1 : 3) in a one-step solution process was later successfully extended to the planar configuration, with substantially different film properties.[91] It is reported that the mixed halide $MAPbI_{3-x}Cl_x$ exhibits improved film characteristics, *e.g.* more compact and increased grain size, when compared with the pure iodide $MAPbI_3$ perovskite. Also, the carrier behavior of the $MAPbI_{3-x}Cl_x$ film is improved, with a carrier lifetime of over 100 ns, in contrast to $MAPbI_3$ of around 10 ns.[83] Thus, the dramatically different film quality of the perovskite films, originated from the stoichiometry of the precursors, leads to their different device performances.

Further studies on film formation based on stoichiometry effects have also been conducted, in terms of the phase, the underlying reaction, and the possible byproducts. Interestingly, the $MAPbI_{3-x}Cl_x$ obtained from $PbCl_2$: MAI (1 : 3) solution and the $MAPbI_3$ from PbI_2 : MAI (1 : 1) solution exhibited nearly identical XRD patterns, which mainly consist of the $MAPbI_3$ phase. This strongly suggests that an intensive ion exchange between I and Cl occurs during the perovskite formation, as described in eqn (1).[50] Other phases, including PbI_2 and $MAPbCl_3$, coexisting with the $MAPbI_3$ phase were observed in the films derived from $PbCl_2$: MAI (1 : 3) solution.[92] These observations are also consistent with previous studies on the $MASnX_3$-perovskite crystal, where iodide and chloride elements cannot form a mixed $MASnI_{3-x}Cl_x$ phase, as a result of the extremely low solubility of chloride in the $MASnI_3$ phase.[93] In addition, the iodide-rich condition would lead to a high density deep defect (I_{Pb}) and the Cl-based precursor can suppress the I_{Pb} defect formation.[94] Therefore, to form a $MAPbI_3$ perovskite phase with less deep defects, three times the amount of MAI to $PbCl_2$ is required for slightly iodide poor conditions. Any stoichiometry deviation from 1 : 3 ($PbCl_2$: MAI) may cause either excessive MAI or unreacted $PbCl_2$ to remain within the film, which can be expected to degrade their resulting optoelectronic performance.

$$3MAI + PbCl_2 \rightarrow MAPbI_3 + 2MACl \quad (1)$$
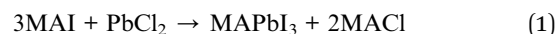
Another impurity in the film is the byproduct MACl, formed according to eqn (1). However, XRD patterns do not show any obvious MACl phase, possibly due to the sublimation or decomposition of most MACl and formation of the $MAPbCl_3$ phase which is observed by XRD.[92] While in almost all cases, $MAPbI_{3-x}Cl_x$ was used to represent the final product, where the Cl is proved to be in the form of $MAPbCl_3$, and/or is speculated to be dissolved within the $MAPbI_3$.[95] Detailed studies on the non-stoichiometry ratio of the precursors and the amount of the Cl introduced into the perovskite remain under investigation.
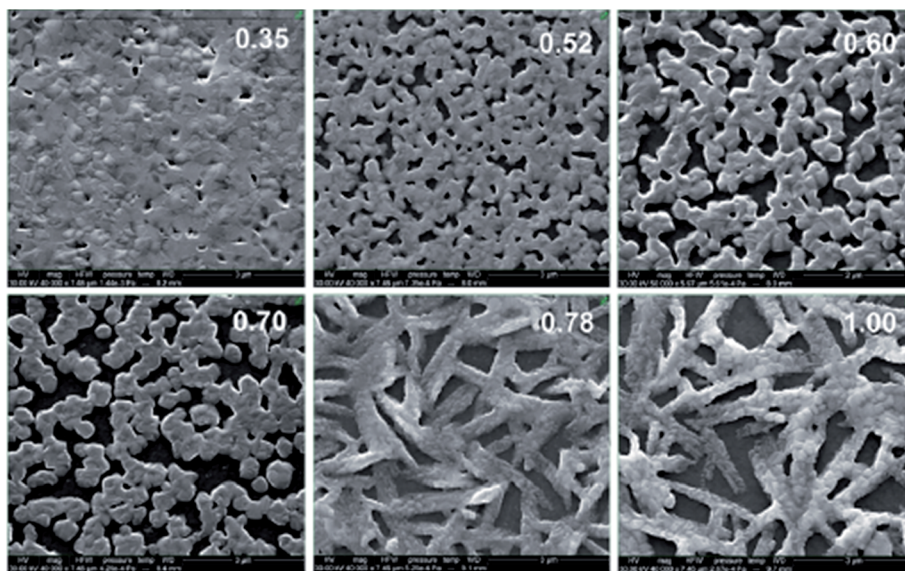
Fig. 9 The top view SEM images of the perovskite films prepared from different mole ratios of PbI$_2$ to MAI dissolved in DMF. Adapted with permission from ref. (34). Copyright 2014 The Royal Society of Chemistry.

Besides the mixed halide MAPbI$_{3-x}$Cl$_X$, a non-stoichiometric solution of PbI$_2$ and MAI is examined with an important role for high performance MAPbI$_3$ based on a one-step solution process method. The best device performance of around 12.2% was demonstrated by using the precursor solution of 0.6–0.7 : 1 mole ratio of PbI$_2$ to MAI in DMF.[34] The authors believed that the residual amounts of PbI$_2$ and MAI in the final film are different because of their different affinities to the substrate, and the non-stoichiometric precursor solution is required for MAPbI$_3$ film formation. A higher PbI$_2$ to MAI ratio (>0.8 : 1) in the precursor leads to the formation of microfibers in the film, which increases the film roughness significantly. The morphology transformations as viewed under SEM are shown in Fig. 9. In addition, the MAPbI$_3$ from lower PbI$_2$ to MAI ratios (<0.6 : 1) did not exhibit the typical photoluminescence peak and absorption edge. In sum, the MA (Pb,Sn)X$_3$ film was largely affected by the stoichiometry of the precursor solution, resulting in a long carrier lifetime and compact grains in the films upon introducing Cl and better film coverage with the non-stoichiometry method. It is also believed that introducing Cl could form an intermediate complex to reduce the interface energy and enhance the film formation in the one step solution process.

3.2 Heat treatment

In general, thermal annealing is an essential step to initiate or accelerate the reaction between the molecules, as well as the film formation. With regard to hybrid perovskite materials, a delicate control of heat treatment is needed due to the fast reaction rate between the organic–inorganic component, and their various phases in the low temperature range. Eperon *et al.* investigated the properties of mixed halide perovskite MAPbI$_{3-X}$Cl$_X$ planar films based on one-step solution processing at different annealing temperatures.[65] The perovskite films

with different film thicknesses deposited on the compact TiO$_2$ ETL layers were annealed at different temperatures ranging from 90 °C to 170 °C. The authors observed that the higher the annealing temperature, the lower the film surface coverage, as shown in Fig. 10(a and b). Also, both the increased initial film thickness of the perovskite and compact TiO$_2$ layers could improve the surface coverage of final perovskite films. The resulting device performances demonstrated that a higher J_{SC} can be achieved from the film with higher coverage because of its increased light absorption capabilities.[65]

The controlled annealing temperature produces a perovskite layer with different surface coverage, which was further employed to construct semitransparent perovskite solar cells with controlled transmission properties. Dualeh *et al.* reported the annealing effects in a single-step solution processed mixed MAPbI$_{3-X}$Cl$_X$ perovskite based on a mesoporous structure.[96] The crystallinity, optical, and electrical properties of the film were examined by annealing the identical films in a wide temperature range (25–200 °C) and the XRD spectra are shown in Fig. 10(c). The authors demonstrated that densely interconnected perovskite films can be obtained under 80 °C or 100 °C for 3 h or 0.75 h annealing, respectively. When the film experienced lower temperature (<80 °C) annealing, the perovskite phase formation was obviously hindered. For example, a film obtained by annealing at 60 °C for 20 h exhibits poor absorption, low film coverage, imperfect crystallinity, and impure phases. Further prolonging the annealing time under lower temperature will not provide any advantage for future application and fabrication. On the other hand, perovskite films annealed using higher temperatures (>100 °C) will produce the secondary phase PbI$_2$, likely originating from the decomposition of MAPbI$_3$ or possibly the exchange of iodide with the PbCl$_2$ precursor film. This is well matched with the proposed additional side reactions, as shown in eqn (2) and (3).
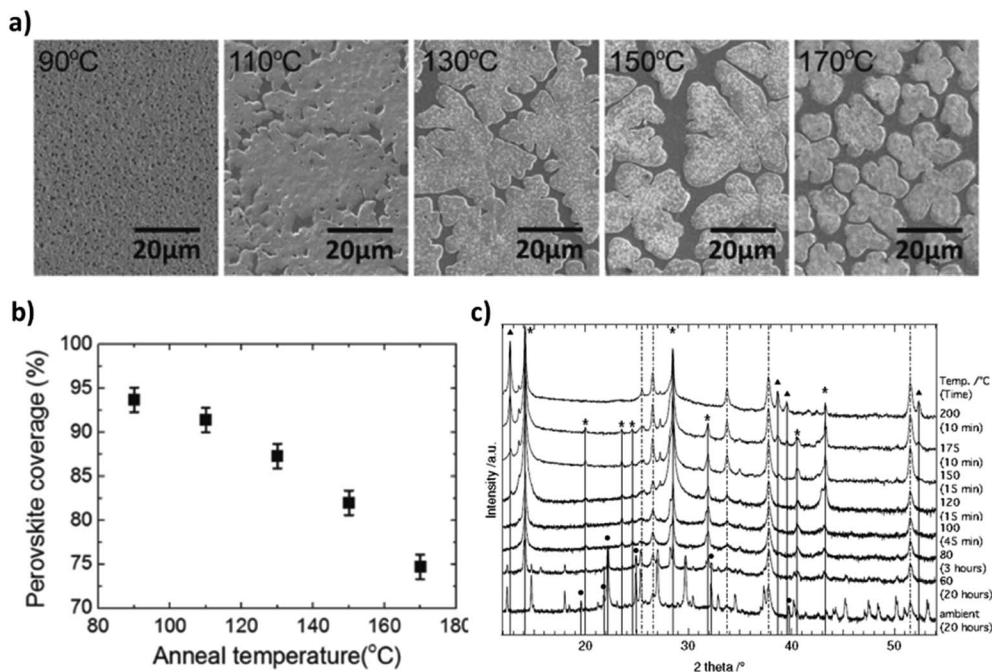
Fig. 10 One-step solution processed perovskite films annealed under different temperatures: (a) the top view SEM images; (b) the surface coverage; (c) the XRD spectra of perovskite films obtained under different annealing temperatures and time. Adapted with permission from ref. (65 and 96). Copyright 2013 Wiley.

$$3MAI + PbCl_2 \rightarrow PbI_2 + 2MACl + MAI \qquad (2)$$

$$MAPbI_3 \rightarrow PbI_2 + CH_3NH_2 + HI \qquad (3)$$

Controlling the thermal annealing process is also a crucial factor to achieving high performance in the case of the VASP method as reported by Chen *et al.* and the stacked precursor method as reported by Xiao *et al.*[33,41] In the VASP process, MAI vapor is generated under 150 °C, with an excessive amount of MAI powder being required to maintain the MAI vapor pressure in the reaction chamber. In the stacked precursor interdiffusion process, an annealing temperature of 100 °C was used to enhance the interdiffusion between layers and to prevent MAI from escaping the film surface. Using overly high or low processing temperatures will cause undesired film qualities, as a result of relatively slow reactions or side/decomposition reactions as shown in eqn (2) and (3). In both cases, the annealing temperature has only a minor effect regarding the surface coverage of the films, because of the presence of the pre-formed conformal PbI_2 films that are used as templates.

These experimental observations are consistent with the results suggested by theoretical calculations. Recently, Burlakov *et al.* developed a theoretical model to investigate the MAPbI$_{3-x}$Cl$_X$ film formation based on one-step solution processing.[97] The authors found the unfavorable interface between the perovskite film and the substrate and also pointed out a potential processing window for the community. Moreover, a hot-casting process was recently demonstrated using a hot solution (70 °C) deposited onto 50–200 °C substrates by Nie *et al.*, and more than millimeter-scale crystalline grains were

achieved on the PEDOT:PSS layer.[98] Additional theoretical modeling could also be helpful in finding the best combination of the substrate material and the perovskite precursor for high quality film formation and for the design of a corresponding facile fabrication process.

3.3 Additives

The inclusion of small amounts of chemical additives in perovskite precursor solutions have been reported to provide advantages in terms of crystallinity, film coverage, and the resulting device performance. Adopted from organic photovoltaics research efforts,[99] Liang *et al.* added 1% of 1,8-diiodooctane (DIO) into a perovskite precursor solution and demonstrated an increase in device performance in contrast to devices based on precursors without any additives.[100] The films exhibited improved surface coverage and crystallinity as observed using SEM and XRD, respectively. They speculated that the temporary coplanar chelation of Pb^{2+} with DIO, as I$^-$ ligands reside in axial octahedral positions on Pb^{2+}, enhances the solubility of PbCl_2 in DMF. The proposed mechanism was represented using the schematic diagram shown in Fig. 11(a). The chelation efficiency could be further modulated to control the film growth.

Zhao *et al.* incorporated excess MACl into the PbI_2 + MAI precursor solution in an effort to module the formation of the perovskite phase.[101] The authors observed that with the added MACl, MAPbI_3 exhibited conformal characteristics other than undesirable branch type crystals which are observed in Fig. 11(b–e). By adjusting the ratios of PbI_2, MAI, and MACl in
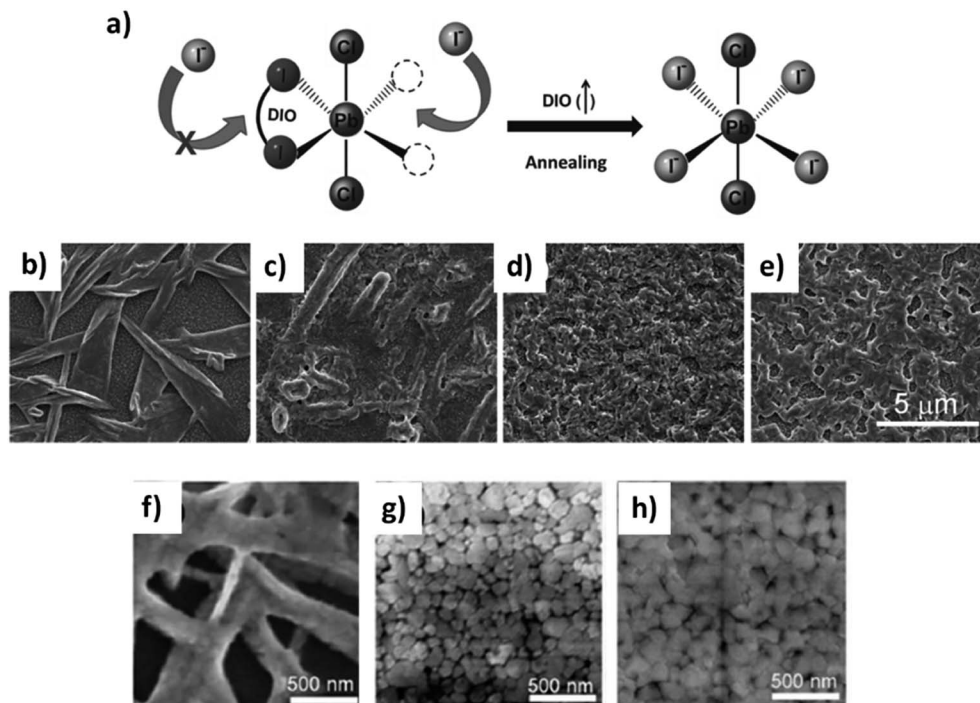
Fig. 11 (a) The proposed mechanism of DIO interaction with the PbX_2 complex. The top view SEM images: (b–e) perovskite films from different amounts of MACl treatment; (f–g) perovskite films from different amounts of NH_4Cl treatment. Adapted with permission from ref. (100–102). Copyright 2014 Wiley, 2014 American Chemical Society, 2014 The Royal Society of Chemistry.

the precursor, it is found that $MAPbCl_3$ and $MAI\text{-}PbI_2\text{-}xMACl$ were potentially present as intermediate states during $MAPbI_{3-X}Cl_X$ formation. This observation also coincides with previous findings that MACl served as a sacrificial agent and decomposed during thermal annealing. The device performance confirms the positive effect coming from MACl addition. Moreover, Ding *et al.* reported a high fill factor perovskite solar cell based on NH_4Cl as an additive in the PbI_2–MAI precursor.[102] Better crystallinity, well-defined morphology, and improved device performance were evident, similar to films that use DIO or MACl as additives. The mechanism by which the NH_4Cl additive brings about improvements is still unclear at present. However, it is believed that NH_4Cl acts in a similar fashion to MACl in perovskite film growth as shown in Fig. 11(f–h). These results suggest that the introduction of additives into the precursor film could be an effective way in controlling the film growth and subsequently enhancing the device performance.

3.4 Atmospheres

Generally, perovskite films are deposited and annealed in nitrogen or dry air glove boxes with H_2O levels less than 5 ppm, as the presence of moisture was deduced to deteriorate the perovskite film. However, in a recent report, Zhou *et al.* found that perovskite films annealed in a mild moisture environment (∼30% humidity) could in fact improve film properties significantly.[35] The growth mechanism was examined by XRD and SEM characterization, where stronger $MAPbCl_3$ peaks during the film transformation were observed (as shown in Fig. 12) compared with the film that was fabricated with minimal humidity. It is speculated that the moisture could enhance film formation by partially dissolving the reaction species and accelerating mass transport within the film. The time-resolved photoluminescence measurements demonstrated an improvement in carrier lifetime of the perovskite films by almost 2 times, as well as a dramatic improvement in the V_{OC} (from 1.02 V to 1.11 V). You *et al.* also reported the moisture assisted perovskite film growth on PSS:PEDOT. Compared to other atmospheric conditions, perovskite films annealed in ambient airimproved crystallinity and larger grain sizes were obtained, as evidenced by XRD and SEM.[103] Moisture could possibly promote the movement of organic species and accelerate the grain growth, resulting in less pinholes in the films. However, the films annealed under high moisture conditions showed obvious PbI_2 peaks, as a result of the decomposition of organic species. These results indicate that a controlled atmosphere during the film formation will result in high performance perovskite devices, and further examination of the effects of different atmospheres is still under investigation.

3.5 Solvent engineering

Solvent plays a critical role in all kinds of solution processes and determines the quality of hybrid perovskite films. In a typical one-step deposition process, a mixture of two different precursors (*e.g.* methylammonium iodide and lead halides) is used. Due to the distinct nature of organic and inorganic precursors, however, the selection of solvents with sufficient solubility for both components is limited. Currently, DMF, DMSO, GBL, and their mixtures are used in most situations.
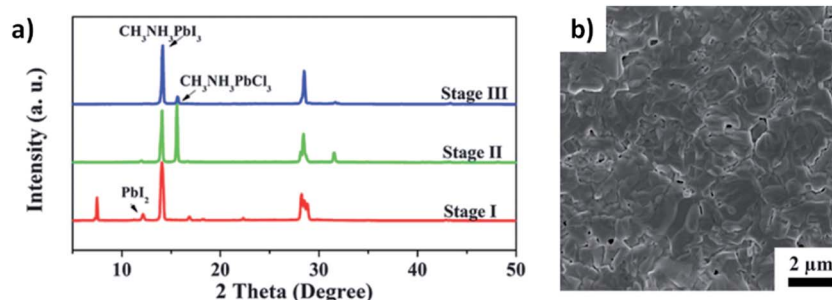
Fig. 12 (a) The XRD spectra of perovskite films annealed under 90–105 °C for different time; (b) the top view SEM images of the perovskite film annealed for 85 min under mild moisture conditions. Adapted with permission from ref. (35). Copyright 2014 American Association for the Advancement of Science.

In the original reports, in which the perovskite layer was deposited on a mesoporous TiO$_2$ scaffold, GBL was employed as the solvent. As shown in Fig. 13, it resulted in effective pore filling of the perovskite on the mesoporous TiO$_2$ electrodes.[87] By tuning the concentration of the precursors, an overlayer is formed on the top of the mesoporous structure, as shown in Fig. 13, where several micrometer-sized MAPbI$_3$ islands are densely formed on top of the mesoporous TiO$_2$ film.[53]

DMF was first used by the Snaith group to deposit the perovskite films on mesoporous Al$_2$O$_3$ scaffolds.[50] Later, it was adopted to fabricate perovskite solar cells with planar geometry.[62] DMF exhibits a relatively low boiling point (154 °C) compared to that of GBL (204 °C), which facilitates the film formation. With the adoption of DMF for constructing the perovskite film by the overall research community, it was discovered that DMF is able to coordinate with lead halide, creating an intermediate phase during film growth which is closely related to a hybrid film reconstruction process.[35] The reconstruction process leads to improved film optoelectronic properties and device performance.

By employing DMF as the solvent, the solution of precursors reaches a maximum concentration of ∼1 M at elevated temperatures. However, due to the extremely high growth rate of perovskites, thin films with pinhole and moderate surface coverage via the one-step DMF based solution process are usually observed. An alternative solvent, DMSO, enables precursor solutions to be prepared with considerably enhanced concentrations of the perovskite materials, up to 60 wt%.[104]

Highly concentrated precursors allow for the deposition of optically dense perovskite films, which results in increased device performance.

Mixed solvents have been reported to improve the morphology of the perovskite film.[105] It is observed that use of a DMF and GBL mixture produces smooth perovskite films and uniform crystal domains with small grain sizes on PEDOT:PSS substrates, which have been shown to improve the interfacial contact. The combination of DMSO/GBL is another choice for fabricating perovskite films of high quality. Further studies show a MAI–PbI$_2$–DMSO complex during the film formation where DMSO/GBL mixed solvents was employed.[54] Perovskite films were deposited on a mesoporous TiO$_2$ layer via spin-coating the mixed solution, followed by a toluene drip while spinning, as shown in Fig. 14(a and b). The film showed compact polycrystalline texture, with the grain size up to several hundred nanometers. The toluene droplets lead to immediate freezing of the constituents during spinning via quick removal of the excess DMSO solvent and rapid formation of the MAI–PbI$_2$–DMSO phase, leaving a uniform and transparent layer. With this method, the perovskite films can also be fabricated on PEDOT:PSS substrates.[106]

A similar solvent-induced processing technique has also been adapted to fabricate perovskite layers in planar geometry. After spin-coating a DMF solution of MAPbI$_3$, the wet film was immediately exposed to chlorobenzene to induce fast crystallization as shown in Fig. 14(c).[107] This resulted in films with flat and compact polygon grain features up to microns across. This characteristic leads to improved charge transport properties within the perovskite film. Interestingly, it is found that the morphologies of the resulting films are closely related to the delay time when chlorobenzene is introduced during spin-coating. When evaporation of the residual solvent occurs significantly and concentrates the perovskite solution, a dense and uniform film was formed by the introduction of the second solvent. In this study, 12 solvents were investigated, where the addition of chlorobenzene, benzene, xylene, and toluene leads to uniform films over the entire substrate. Therefore, the solvents either from the precursor solution or induced during the processing substantially influence the molecule/species interaction within the system, and the subsequent film quality.
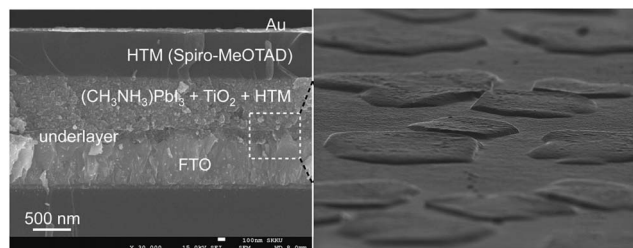

Fig. 13 (Left) Cross-section and (Right) surface SEM images of the MAPbI$_3$-coated mp-TiO$_2$ film. Adapted with permission from ref. (53 and 87). Copyright 2013 Nature Publishing Group.
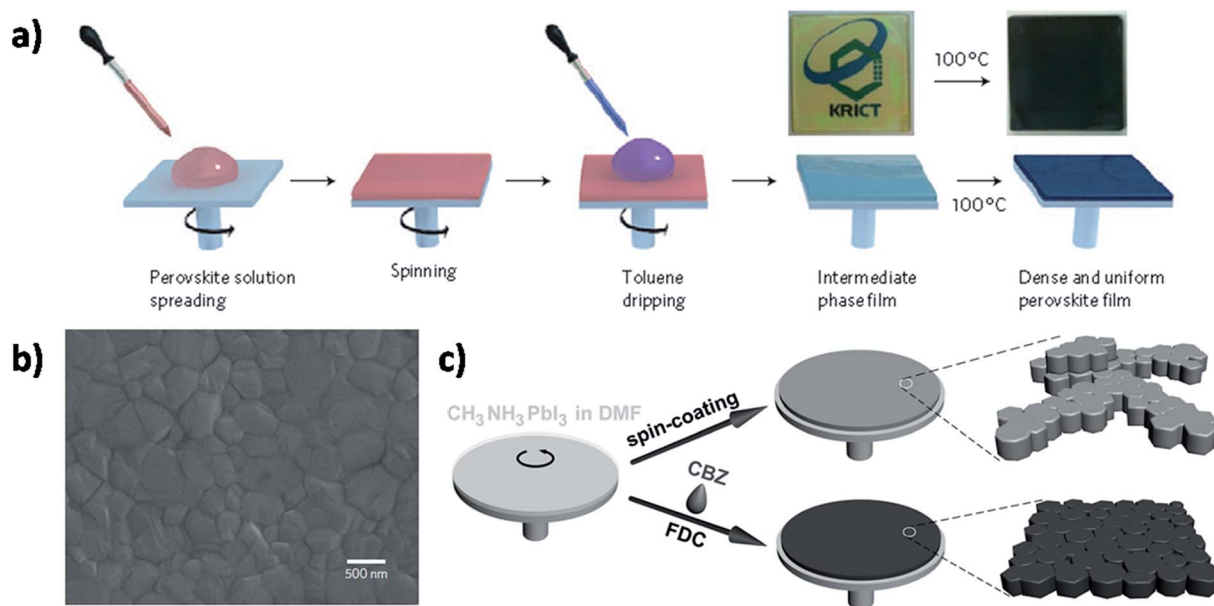
Fig. 14 (a) Schematic illustration of perovskite films prepared from DMSO/GBL mixed solvent and dripped with toluene and (b) the top view SEM of the perovskite film from this method. (c) Schematic illustration of the perovskite film deposited and immediately treated with chlorobenzene. Adapted with permission from ref. (54 and 107). Copyright 2014 Nature Publishing Group, 2014 Wiley.
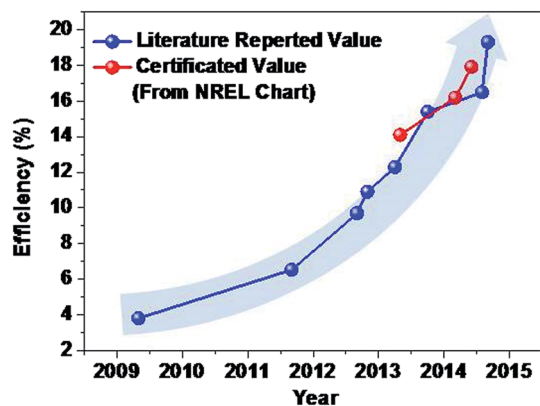

Fig. 15 Efficiency trend of MAPbX$_3$-based perovskite solar cells collected from the literature reported values and NREL report chart.

4. Device performance

The device performances of hybrid perovskite solar cells have exhibited remarkable growth in the past several years. The power conversion efficiency has been pushed from 3.8% to 19.3% based on interface design and controlled perovskite film growth. Here, we discuss several of the main milestone findings in perovskite research. In 2008 and 2009, Kojima *et al.* used MAPbI$_3$ and MAPbBr$_3$ as the light harvesting layer in a DSSC configuration, and achieved a PCE of about 3.8%.[61] Later Im *et al.* optimized the fabrication conditions with using MAPbI$_3$ quantum dots, delivering a 6.5% PCE.[108] The optimized TiO$_2$ layer thickness provided the significant J_{SC} enhancement. However, MAPbX$_3$ (X = Br, I) was found to dissolve in polar solvents, rendering the perovskite in a solar cell with a liquid electrolyte layer unstable. This instability was eventually resolved by adapting solid hole conductors in place of the liquid redox electrolyte. A PCE as high as 9.7% was later achieved by the solid state structure, even when perovskites were deposited onto a mesoporous TiO$_2$ scaffold with only sub-micrometer thickness.[87] Subsequently, an insulating Al$_2$O$_3$ network was used to replace conducting nanoporous TiO$_2$. Using a mixed MAPbI$_{3-X}$Cl$_X$ as the sensitizer, an improved open-circuit voltage (V_{OC}) was demonstrated, and the reported efficiency boosted to 10.9%.[50]

In 2013, a two-step procedure of MAI intercalation following layered PbI$_2$ deposition resulted in a PCE of 15% and a certified PCE of 14.1%.[55] Similar results using a planar cell configuration to eliminate the mesoporous scaffolding and a MAPbI$_{3-X}$Cl$_X$ absorber deposited by a two-source thermal evaporation produced a reported efficiency of 15.4%.[32] Jeon *et al.* demonstrated the solvent engineering method as discussed in the previous section to achieve dense perovskite films and a 16.2% PCE was reported based on this process modification.[54]

The highest PCE obtained by a significant margin was confirmed from the Korean Research Institute of Chemical Technology (KRICT) at 17.9%.[1] There are additional reports of equally high or higher efficiency values, although difficulties regarding packaging and encapsulation have reduced the number of these reports that result in certified efficiency values. As a recent example, our group has produced cells with a PCE of 19.3% through careful interface design and film formation control. The PCE trend of each of these reported values is shown in Fig. 15.[35]

All the aforementioned perovskite solar cells are based on the regular structure, (*i.e.* FTO/TiO$_2$/perovskite/Spiro-OMeTAD/Au). Recently, cells that make use of an inverted structure (*i.e.*
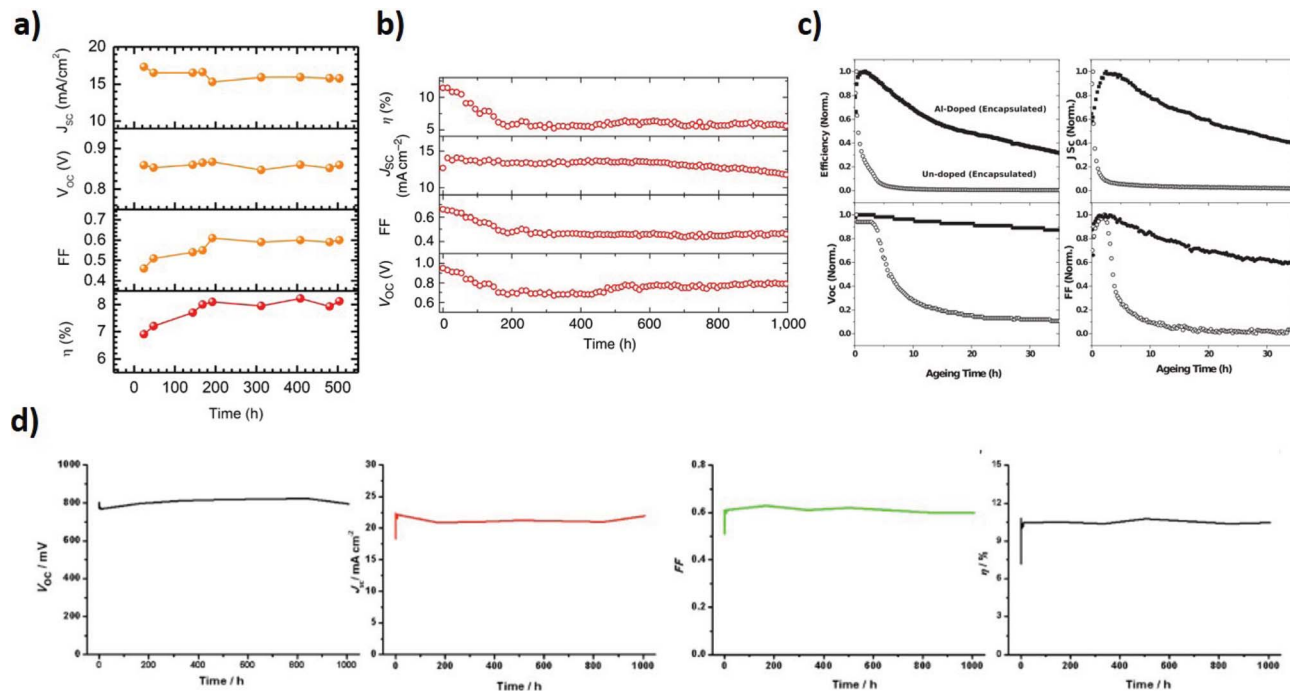
Fig. 16 Long term stability tests of perovskite devices and the photovoltaic parameters: (a) all solid state MAPbI$_3$ perovskite devices without encapsulation under white light illumination for over 500 h in air; (b) replacing TiO$_2$ with Al$_2$O$_3$ to prevent the photochemical reaction by UV light, the encapsulated device stabilized after 200 h under 40 °C with full spectrum illumination; (c) Al doped TiO$_2$ was used to reduce the surface defects of TiO$_2$, the encapsulated devices were performed to show an improved stability. (d) HTL free, (5-AVA)$_X$(MA)$_{1-X}$PbI$_3$ perovskite device based on ZrO$_2$ as the mesoporous scaffold and carbon as the electrode demonstrated more than 1008 h stability under full sunlight illumination without encapsulation. Adapted with permission from ref. (77, 87, 114 and 116). Copyright 2014 Nature Publishing Group, 2014 Wiley, 2014 American Association for the Advancement of Science.

ITO/PEDOT:PSS/perovskite/PCBM/Al) have begun attracting attention as well. This device structure was first reported by Jeng *et al.* with a PCE of 4%.[62] At the beginning of 2014, several groups simultaneously reported efficiencies surpassing 10%.[40,91] Recently, the efficiency has been pushed to above 17%.[41,109] We believe that in the near future the efficiency of this inverted structure could catch up with the regular structure.

Perovskite solar cells hold promise as a low-cost, highly efficient alternative to conventional semiconductor-based solar cells. We believe that the perovskite solar cell PCE can reach beyond 20% for the single junction and even 30% PCE may eventually be possible when tandem structures are implemented by integrating suitable low bandgap material systems such as CIGS or Si.[2,110–113]

5. Stability

Perovskite solar cells have been demonstrated with promising PCEs recently. However, in practical applications, the devices suffer from extreme instability with water, light and heat. This is due to the instability of both the perovskite material itself, as well as the transport materials used in the device architecture. For MAPbX$_3$-based perovskite materials, the organic species are easy to escape from the film by storing in the environment containing moisture, and during heat treatment. Additionally, the phase transformation of MAPbX$_3$ materials occurred at 330

K, as mentioned in Section 2.4, further increasing the instability under solar cell working conditions. Besides perovskite itself, the transporting layers, including the ETL, *e.g.* TiO$_2$ and PCBM, and HTL, *e.g.* Spiro-OMeTAD and PEDOT:PSS also cause the instability of perovskite solar cells. For example, the TiO$_2$ layer is sensitive to ultraviolet light, and PCBM is not stable in air. For HTL, the use of Spiro-OMeTAD required an additive, *e.g.* 4-*tert*-butylpyridine (tBP), which can react with perovskite materials. With regard to PEDOT:PSS, its acidic nature also becomes a concern for the long-term stability of solar cells.

In a previous work, Im *et al.* pointed out the instability of the perovskite materials working as the dye in DSSC, where the efficiency degraded to 80% of its original performance in a short period of 10 min under 1 sun illumination.[108] The perovskite was found to dissolve into the electrolyte gradually, as a result of the hygroscopic nature of organic species, such as MAI. To prevent the degradation induced by solvents, Kim *et al.* improved the stability by fabricating perovskite solar cells based on solid state. Under continuous white light illumination for over 500 h in air, the perovskite devices without encapsulation maintained a device PCE as high as 8% as shown in Fig. 16(a).[87] Leijtens *et al.* further noticed that the mesoporous TiO$_2$ could cause the instability of the perovskite solar cell, where desorption of surface-adsorbed oxygen under UV-illumination causes deep traps and reduces the device performance. The replacement of TiO$_2$ with Al$_2$O$_3$ can provide a better light stability.

Thus, more than 1000 h full spectrum illumination at 40 °C was applied to the perovskite solar cell with encapsulation, and the PCE is stabilized after 200 h of the test with ∼40% degradation as shown in Fig. 16(b).[114] Both UV filter and Al doped TiO_2 were employed to further improve the stability by preventing the UV induced photocatalysis and desorption of oxygen on the TiO_2 surface as shown in Fig. 16(c).[115,116] To improve the stability of the interface between perovskite/HTL, Li *et al.* incorporated montmorillonite (MMT) as a buffer layer between Spiro-OMe-TAD and perovskite to prevent the corrosion induced by tBP.[117] Nguyen *et al.* synthesized Spiro(TFSI)$_2$ to replace Spiro-OMe-TAD, where it can avoid the doping process for the HTL materials.[118] To further improve the stability, one of the most striking approaches is based on incorporating 5-AVA iodide into the commonly used precursor solution (PbI_2 and MAI mixture), combined with carbon electrode.[77] The carbon electrode is assumed to collect photogenerated carriers, and act as the protection layer as well. The introduction of 5-AVA iodide dopant was believed to lower the defect concentration providing better pore-filling in the scaffold. Moreover, the structure does not require any HTL, which also render an improved stability for the corresponding perovskite solar cell. Around 10% PCE was obtained for the device and stabilized for more than 1008 h under 1 sun illumination at room temperature without encapsulation as shown in Fig. 16(d). More recently, an interesting work was done by Smith *et al.* by changing the structure of perovskite materials from three dimensional to two dimensional structure. The $C_6H_5(CH_2)_2NH_3^+$ (PEA) was used to replace certain amount of MAI to form layered perovskite (PEA)$_2$(MA)$_2$[Pb$_3$I$_{10}$].[119] There is no obvious phase segregation after exposure to moisture for 46 days. It is well recognized that the long-term stability of the device can not only rely on encapsulation technology, but also on modification of the perovskite materials' intrinsic properties and designing stable ETL and HTL materials. Substantial efforts on molecular design of the organic species and the corresponding structural change from different organic species are expected to further improve the device stability of perovskite solar cells.

6. Conclusion

Film formation of the absorber layer is the key factor that determines the eventual performance of a perovskite solar cell. The successful demonstration of high performance perovskite solar cells based on mesoporous oxide scaffolds has proven the importance of the film quality, *e.g.* surface coverage and roughness, loading percentage, and crystallinity. However, a high temperature annealing process is needed to fabricate the mesoporous scaffold, which may increase the processing complexity and cost, and decrease the compatibility of implementing a high performance flexible product, as well as integrating tandem cells into existing technologies, *e.g.* Si and CIGS modules.

Approaches based on a planar device configuration simplify the fabrication of high performance devices. These methods rely on the careful control of the reaction between the organic and inorganic species, and the formation of a continuous film with a large average grain size. Various parameters including chemical stoichiometry, annealing temperature and time, deposition solvent(s), processing environment, and additives, play an instrumental role in improving the film quality. This simplified configuration and its accompanying relaxation of processing conditions further promises lower processing costs and simple implementation of this type of device.

Numerous research efforts within the perovskite solar cell community are ongoing in the hope of approaching practical commercialization in the coming years. On-going efficiency and stability improvements are expected, with an unprecedented level of progress in film formation and the corresponding understanding of materials and processes. The advantage of perovskite solar cells over existing solar technology lies within their excellent optical and electrical properties, low cost raw materials, and facile film and device fabrication. It is anticipated that the demonstration of new solar technologies based on perovskites, or the integration of an established manufacturing method that uses both perovskite and existing technologies are particularly promising for the future photovoltaic market.

Acknowledgements

References

1 http://www.nrel.gov/ncpv/images/efficiency_chart.jpg.

2 H. J. Snaith, *J. Phys. Chem. Lett.*, 2013, **4**, 3623–3630.

3 M. A. Green, K. Emery, Y. Hishikawa, W. Warta and E. D. Dunlop, *Prog. Photovoltaics*, 2014, **22**, 1–9.

4 S. Sun, T. Salim, N. Mathews, M. Duchamp, C. Boothroyd, G. Xing, T. C. Sum and Y. M. Lam, *Energy Environ. Sci.*, 2014, **7**, 399–407.

5 C. Wehrenfennig, M. Liu, H. J. Snaith, M. B. Johnston and L. M. Herz, *J. Phys. Chem. Lett.*, 2014, **5**, 1300–1306.

6 G. Xing, N. Mathews, S. Sun, S. S. Lim, Y. M. Lam, M. Grätzel, S. Mhaisalkar and T. C. Sum, *Science*, 2013, **342**, 344–347.

7 Z. Ku, Y. Rong, M. Xu, T. Liu and H. Han, *Sci. Rep.*, 2013, **3**, 3132.

8 J. Mats and L. Peter, *J. Phys.: Condens. Matter*, 2008, **20**, 264001.

9 D. V. Taylor and D. Damjanovic, *Appl. Phys. Lett.*, 2000, **76**, 1615–1617.

10 J. Hejtmánek, Z. Jirák, M. Maryško, C. Martin, A. Maignan, M. Hervieu and B. Raveau, *Phys. Rev. B: Condens. Matter Mater. Phys.*, 1999, **60**, 14057–14065.

11 D. B. Mitzi, K. Chondroudis and C. R. Kagan, *IBM J. Res. Dev.*, 2001, **45**, 29–45.

12 T. He, Q. Huang, A. P. Ramirez, Y. Wang, K. A. Regan, N. Rogado, M. A. Hayward, M. K. Haas, J. S. Slusky, K. Inumara, H. W. Zandbergen, N. P. Ong and R. J. Cava, *Nature*, 2001, **411**, 54–56.

13 D. B. Mitzi, *Inorg. Chem.*, 2000, **39**, 6107–6113.

14 D. B. Mitzi, *Prog. Inorg. Chem.*, 2007, **48**, 1–121.

15 D. B. Mitzi, C. D. Dimitrakopoulos and L. L. Kosbar, *Chem. Mater.*, 2001, **13**, 3728–3740.

16 D. B. Mitzi, *J. Chem. Soc., Dalton Trans.*, 2001, 1–12.

17 M. A. Green, A. Ho-Baillie and H. J. Snaith, *Nat. Photonics*, 2014, **8**, 506–514.

18 S. Kazim, M. K. Nazeeruddin, M. Grätzel and S. Ahmad, *Angew. Chem., Int. Ed.*, 2014, **53**, 2812–2824.

19 N.-G. Park, *J. Phys. Chem. Lett.*, 2013, **4**, 2423–2429.

20 W.-J. Yin, T. Shi and Y. Yan, *Adv. Mater.*, 2014, **26**, 4653–4658.

21 H. J. Snaith and M. Gratzel, *Adv. Mater.*, 2007, **19**, 3643–3647.

22 J. Even, L. Pedesseau and C. Katan, Proc. SPIE, Photonics Sol. Energy Syst. V, 91400Y, May 15, 2014.

23 J. Kim, S.-H. Lee, J. H. Lee and K.-H. Hong, *J. Phys. Chem. Lett.*, 2014, **5**, 1312–1317.

24 P. Docampo, S. Guldin, T. Leijtens, N. K. Noel, U. Steiner and H. J. Snaith, *Adv. Mater.*, 2014, **26**, 4013–4030.

25 K. L. Chopra, P. D. Paulson and V. Dutta, *Prog. Photovoltaics*, 2004, **12**, 69–92.

26 L. Dou, J. You, Z. Hong, Z. Xu, G. Li, R. A. Street and Y. Yang, *Adv. Mater.*, 2013, **25**, 6642–6671.

27 H. Zhou, W.-C. Hsu, H.-S. Duan, B. Bob, W. Yang, T.-B. Song, C.-J. Hsu and Y. Yang, *Energy Environ. Sci.*, 2013, **6**, 2822–2838.

28 S. Lv, L. Han, J. Xiao, L. Zhu, J. Shi, H. Wei, Y. Xu, J. Dong, X. Xu, D. Li, S. Wang, Y. Luo, Q. Meng and X. Li, *Chem. Commun.*, 2014, **50**, 6931–6934.

29 J. M. Ball, M. M. Lee, A. Hey and H. J. Snaith, *Energy Environ. Sci.*, 2013, **6**, 1739–1743.

30 A. Marchioro, J. Teuscher, D. Friedrich, M. Kunst, R. van de Krol, T. Moehl, M. Gratzel and J.-E. Moser, *Nat. Photonics*, 2014, **8**, 250–255.

31 M. H. Kumar, N. Yantara, S. Dharani, M. Graetzel, S. Mhaisalkar, P. P. Boix and N. Mathews, *Chem. Commun.*, 2013, **49**, 11089–11091.

32 M. Liu, M. B. Johnston and H. J. Snaith, *Nature*, 2013, **501**, 395–398.

33 Q. Chen, H. Zhou, Z. Hong, S. Luo, H.-S. Duan, H.-H. Wang, Y. Liu, G. Li and Y. Yang, *J. Am. Chem. Soc.*, 2013, **136**, 622–625.

34 Q. Wang, Q. Dong, Z. Xiao, Y. Yuan and J. Huang, *Energy Environ. Sci.*, 2014, **7**, 2359–2365.

35 H. Zhou, Q. Chen, G. Li, S. Luo, T.-B. Song, H.-S. Duan, Z. Hong, J. You, Y. Liu and Y. Yang, *Science*, 2014, **345**, 542–546.

36 F. Brivio, A. B. Walker and A. Walsh, *APL Mater.*, 2013, **1**, 042111.

37 Y. Chang, C. Park and K. Matsuishi, *J. Korean Phys. Soc.*, 2004, **44**, 889–893.

38 Z. Cheng and J. Lin, *CrystEngComm*, 2010, **12**, 2646–2662.

39 V. Gonzalez-Pedro, E. J. Juárez-Pérez, W. S. Arsyad, E. M. Barea, F. Fabregat-Santiago, I. Mora-Sero and J. Bisquert, *Nano Lett.*, 2014, **14**, 888–893.

40 J. You, Z. Hong, Y. Yang, Q. Chen, M. Cai, T.-B. Song, C.-C. Chen, S. Lu, Y. Liu, H. Zhou and Y. Yang, *ACS Nano*, 2014, **8**, 1674–1680.

41 Z. Xiao, C. Bi, Y. Shao, Q. Dong, Q. Wang, Y. Yuan, C. Wang, Y. Gao and J. Huang, *Energy Environ. Sci.*, 2014, **7**, 2619–2623.

42 S. A. Kulkarni, T. Baikie, P. P. Boix, N. Yantara, N. Mathews and S. G. Mhaisalkar, *J. Mater. Chem. A*, 2014, **2**, 9221–9225.

43 S. P. Singh and P. Nagarjuna, *Dalton Trans.*, 2014, **43**, 5247–5251.

44 J.-H. Im, H.-S. Kim and N.-G. Park, *APL Mater.*, 2014, **2**, 081510.

45 S. Pang, H. Hu, J. Zhang, S. Lv, Y. Yu, F. Wei, T. Qin, H. Xu, Z. Liu and G. Cui, *Chem. Mater.*, 2014, **26**, 1485–1491.

46 I. Chung, B. Lee, J. Q. He, R. P. H. Chang and M. G. Kanatzidis, *Nature*, 2012, **485**, 486–494.

47 S. Rühle and D. Cahen, *J. Phys. Chem. B*, 2004, **108**, 17946–17951.

48 H. J. Snaith, R. Humphry-Baker, P. Chen, I. Cesar, S. M. Zakeeruddin and M. Gratzel, *Nanotechnology*, 2008, **19**, 424003.

49 C. Gratzel and S. M. Zakeeruddin, *Mater. Today*, 2013, **16**, 11–18.

50 M. M. Lee, J. Teuscher, T. Miyasaka, T. N. Murakami and H. J. Snaith, *Science*, 2012, **338**, 643–647.

51 K.-C. Wang, J.-Y. Jeng, P.-S. Shen, Y.-C. Chang, E. W.-G. Diau, C.-H. Tsai, T.-Y. Chao, H.-C. Hsu, P.-Y. Lin, P. Chen, T.-F. Guo and T.-C. Wen, *Sci. Rep.*, 2014, **4**, 4756.

52 T. Leijtens, B. Lauber, G. E. Eperon, S. D. Stranks and H. J. Snaith, *J. Phys. Chem. Lett.*, 2014, **5**, 1096–1102.

53 J. H. Heo, S. H. Im, J. H. Noh, T. N. Mandal, C.-S. Lim, J. A. Chang, Y. H. Lee, H.-J. Kim, A. Sarkar, K. NazeeruddinMd, M. Gratzel and S. I. Seok, *Nat. Photonics*, 2013, **7**, 486–491.

54 N. J. Jeon, J. H. Noh, Y. C. Kim, W. S. Yang, S. Ryu and S. I. Seok, *Nat. Mater.*, 2014, **13**, 897–903.

55 J. Burschka, N. Pellet, S.-J. Moon, R. Humphry-Baker, P. Gao, M. K. Nazeeruddin and M. Gratzel, *Nature*, 2013, **499**, 316–319.

56 N. Pellet, P. Gao, G. Gregori, T. Y. Yang, M. K. Nazeeruddin, J. Maier and M. Gratzel, *Angew. Chem., Int. Ed. Engl.*, 2014, **53**, 3151–3157.

57 D. Sabba, H. A. Dewi, R. R. Prabhakar, T. Baikie, S. Chen, Y. Du, N. Mathews, P. P. Boix and S. G. Mhaisalkar, *Nanoscale*, 2014, **6**, 13854–13860.

58 J. J. Choi, X. Yang, Z. M. Norman, S. J. L. Billinge and J. S. Owen, *Nano Lett.*, 2013, **14**, 127–133.

59 M. H. Du, *J. Mater. Chem. A*, 2014, **2**, 9091–9098.

60 J. Kruger, R. Plass, L. Cevey, M. Piccirelli, M. Gratzel and U. Bach, *Appl. Phys. Lett.*, 2001, **79**, 2085–2087.

61 A. Kojima, K. Teshima, Y. Shirai and T. Miyasaka, *J. Am. Chem. Soc.*, 2009, **131**, 6050–6051.

62 J.-Y. Jeng, Y.-F. Chiang, M.-H. Lee, S.-R. Peng, T.-F. Guo, P. Chen and T.-C. Wen, *Adv. Mater.*, 2013, **25**, 3727–3732.

63 Y.-F. Chiang, J.-Y. Jeng, M.-H. Lee, S.-R. Peng, P. Chen, T.-F. Guo, T.-C. Wen, Y.-J. Hsu and C.-M. Hsu, *Phys. Chem. Chem. Phys.*, 2014, **16**, 6033–6040.

64 J.-Y. Jeng, K.-C. Chen, T.-Y. Chiang, P.-Y. Lin, T.-D. Tsai, Y.-C. Chang, T.-F. Guo, P. Chen, T.-C. Wen and Y.-J. Hsu, *Adv. Mater.*, 2014, **26**, 4107–4113.

65 G. E. Eperon, V. M. Burlakov, P. Docampo, A. Goriely and H. J. Snaith, *Adv. Funct. Mater.*, 2013, **24**, 151–157.

66 S. D. Chavhan, O. Miguel, H. J. Grande, V. Gonzalez-Pedro, R. S. Sanchez, E. M. Barea, I. Mora-Sero and R. Tena-Zaera, *J. Mater. Chem. A*, 2014, **2**, 12754–12760.

67 D. Liu and T. L. Kelly, *Nat. Photonics*, 2013, **8**, 133–138.

68 C. C. Stoumpos, C. D. Malliakas and M. G. Kanatzidis, *Inorg. Chem.*, 2013, **52**, 9019–9038.

69 D. B. Mitzi, M. Prikas and K. Chondroudis, *Chem. Mater.*, 1999, **11**, 542–544.

70 V. V. Skopenko, V. N. Kokozay, V. R. Polyakov and A. V. Sienkiewicz, *Polyhedron*, 1994, **13**, 15–18.

71 Y. Wu, A. Islam, X. Yang, C. Qin, J. Liu, K. Zhang, W. Peng and L. Han, *Energy Environ. Sci.*, 2014, **7**, 2934–2938.

72 S. Colella, E. Mosconi, P. Fedeli, A. Listorti, F. Gazza, F. Orlandi, P. Ferro, T. Besagni, A. Rizzo, G. Calestani, G. Gigli, F. De Angelis and R. Mosca, *Chem. Mater.*, 2013, **25**, 4613–4618.

73 J. H. Noh, S. H. Im, J. H. Heo, T. N. Mandal and S. I. Seok, *Nano Lett.*, 2013, **13**, 1764–1769.

74 F. Hao, C. C. Stoumpos, D. H. Cao, R. P. H. Chang and M. G. Kanatzidis, *Nat. Photonics*, 2014, **8**, 489–494.

75 F. Hao, C. C. Stoumpos, R. P. Chang and M. G. Kanatzidis, *J. Am. Chem. Soc.*, 2014, **136**, 8094–8099.

76 N. Mercier, *CrystEngComm*, 2005, **7**, 429–432.

77 A. Mei, X. Li, L. Liu, Z. Ku, T. Liu, Y. Rong, M. Xu, M. Hu, J. Chen, Y. Yang, M. Gratzel and H. Han, *Science*, 2014, **345**, 295–298.

78 F. Deschler, M. Price, S. Pathak, L. Klintberg, D. D. Jarausch, R. Higler, S. Huettner, T. Leijtens, S. D. Stranks, H. J. Snaith, M. Atature, R. T. Phillips and R. H. Friend, *J. Phys. Chem. Lett.*, 2014, **5**, 1421–1426.

79 G. Xing, N. Mathews, S. S. Lim, N. Yantara, X. Liu, D. Sabba, M. Grätzel, S. Mhaisalkar and T. C. Sum, *Nat. Mater.*, 2014, **13**, 476–480.

80 W.-J. Yin, T. Shi and Y. Yan, *Appl. Phys. Lett.*, 2014, **104**, 063903.

81 S. De Wolf, J. Holovsky, S.-J. Moon, P. Löper, B. Niesen, M. Ledinsky, F.-J. Haug, J.-H. Yum and C. Ballif, *J. Phys. Chem. Lett.*, 2014, **5**, 1035–1039.

82 E. Edri, S. Kirmayer, S. Mukhopadhyay, K. Gartsman, G. Hodes and D. Cahen, *Nat. Commun.*, 2014, **5**, 3461.

83 S. D. Stranks, G. E. Eperon, G. Grancini, C. Menelaou, M. J. P. Alcocer, T. Leijtens, L. M. Herz, A. Petrozza and H. J. Snaith, *Science*, 2013, **342**, 341–344.

84 A. Sadhanala, F. Deschler, T. H. Thomas, S. E. Dutton, K. C. Goedel, F. C. Hanusch, M. L. Lai, U. Steiner, T. Bein, P. Docampo, D. Cahen and R. H. Friend, *J. Phys. Chem. Lett.*, 2014, **5**, 2501–2505.

85 E. T. Hoke, D. J. Slotcavage, E. R. Dohner, A. R. Bowring, H. I. Karunadasa and M. D. McGehee, *Chem. Sci.*, 2015, **6**, 613–617.

86 B. Suarez, V. Gonzalez-Pedro, T. S. Ripolles, R. S. Sanchez, L. Otero and I. Mora-Sero, *J. Phys. Chem. Lett.*, 2014, **5**, 1628–1635.

87 H. S. Kim, C. R. Lee, J. H. Im, K. B. Lee, T. Moehl, A. Marchioro, S. J. Moon, R. Humphry-Baker, J. H. Yum, J. E. Moser, M. Gratzel and N. G. Park, *Sci. Rep.*, 2012, **2**, 591.

88 J. H. Noh, N. J. Jeon, Y. C. Choi, M. K. Nazeeruddin, M. Grätzel and S. I. Seok, *J. Mater. Chem. A*, 2013, **1**, 11842–11847.

89 P. Docampo, F. Hanusch, S. D. Stranks, M. Döblinger, J. M. Feckl, M. Ehrensperger, N. K. Minar, M. B. Johnston, H. J. Snaith and T. Bein, *Adv. Energy Mater.*, 2014, **4**, 1400355.

90 M. J. Carnie, C. Charbonneau, M. L. Davies, J. Troughton, T. M. Watson, K. Wojciechowski, H. Snaith and D. A. Worsley, *Chem. Commun.*, 2013, **49**, 7893–7895.

91 P. Docampo, J. M. Ball, M. Darwich, G. E. Eperon and H. J. Snaith, *Nat. Commun.*, 2013, **4**, 2761.

92 T.-B. Song, Q. Chen, H. Zhou, S. Luo, Y. Yang, J. You and Y. Yang, *Nano Energy*, 2015, **12**, 494–500.

93 K. Yamada, K. Nakada, Y. Takeuchi, K. Nawa and Y. Yamane, *Bull. Chem. Soc. Jpn.*, 2011, **84**, 926–932.

94 A. Buin, P. Pietsch, J. Xu, O. Voznyy, A. H. Ip, R. Comin and E. H. Sargent, *Nano Lett.*, 2014, **14**, 6281–6286.

95 N. K. Mohammad, P. Gao and M. Gratzel, *Energy Environ. Sci.*, 2014, **7**, 2448–2463.

96 A. Dualeh, N. Tétreault, T. Moehl, P. Gao, M. K. Nazeeruddin and M. Grätzel, *Adv. Funct. Mater.*, 2014, **24**, 3250–3258.

97 V. M. Burlakov, G. E. Eperon, H. J. Snaith, S. J. Chapman and A. Goriely, *Appl. Phys. Lett.*, 2014, **104**, 091602.

98 W. Nie, H. Tsai, R. Asadpour, J.-C. Blancon, A. J. Neukirch, G. Gupta, J. J. Crochet, M. Chhowalla, S. Tretiak, M. A. Alam, H.-L. Wang and A. D. Mohite, *Science*, 2015, **347**, 522–525.

99 J. Peet, J. Y. Kim, N. E. Coates, W. L. Ma, D. Moses, A. J. Heeger and G. C. Bazan, *Nat. Mater.*, 2007, **6**, 497–500.

100 P.-W. Liang, C.-Y. Liao, C.-C. Chueh, F. Zuo, S. T. Williams, X.-K. Xin, J. Lin and A. K. Y. Jen, *Adv. Mater.*, 2014, **26**, 3748–3754.

101 Y. Zhao and K. Zhu, *J. Phys. Chem. C*, 2014, **118**, 9412–9418.

102 C. Zuo and L. Ding, *Nanoscale*, 2014, **6**, 9935–9938.

103 J. You, Y. Yang, Z. Hong, T.-B. Song, L. Meng, Y. Liu, C. Jiang, H. Zhou, W.-H. Chang, G. Li and Y. Yang, *Appl. Phys. Lett.*, 2014, **105**, 183902.

104 B. Conings, L. Baeten, C. De Dobbelaere, J. D'Haen, J. Manca and H.-G. Boyen, *Adv. Mater.*, 2013, **26**, 2041–2046.

105 H.-B. Kim, H. Choi, J. Jeong, S. Kim, B. Walker, S. Song and J. Y. Kim, *Nanoscale*, 2014, **6**, 6679–6683.

106 J. W. Seo, S. Park, Y. C. Kim, N. J. Jeon, J. H. Noh, S. C. Yoon and S. I. Seok, *Energy Environ. Sci.*, 2014, **7**, 2642–2646.

107 M. Xiao, F. Huang, W. Huang, Y. Dkhissi, Y. Zhu, J. Etheridge, A. Gray-Weale, U. Bach, Y.-B. Cheng and L. Spiccia, *Angew. Chem.*, 2014, **126**, 10056–10061.

108 J.-H. Im, C.-R. Lee, J.-W. Lee, S.-W. Park and N.-G. Park, *Nanoscale*, 2011, **3**, 4088–4093.

109 C.-H. Chiang, Z.-L. Tseng and C.-G. Wu, *J. Mater. Chem. A*, 2014, **2**, 15897–15903.

110 I. Bruder, M. Karlsson, F. Eickemeyer, J. Hwang, P. Erk, A. Hagfeldt, J. Weis and N. Pschirer, *Sol. Energy Mater. Sol. Cells*, 2009, **93**, 1896–1899.

111 M. A. Green, Proc. SPIE 8981, Phys. Simul. and Photonic Eng. Photovoltaic Device III, 89810L, March 7, 2014.

112 J. Y. Kim, K. Lee, N. E. Coates, D. Moses, T.-Q. Nguyen, M. Dante and A. J. Heeger, *Science*, 2007, **317**, 222–225.

113 J. You, L. Dou, K. Yoshimura, T. Kato, K. Ohya, T. Moriarty, K. Emery, C.-C. Chen, J. Gao, G. Li and Y. Yang, *Nat. Commun.*, 2013, **4**, 1446.

114 T. Leijtens, G. E. Eperon, S. Pathak, A. Abate, M. M. Lee and H. J. Snaith, *Nat. Commun.*, 2013, **4**, 2885.

115 N. Chander, A. F. Khan, P. S. Chandrasekhar, E. Thouti, S. K. Swami, V. Dutta and V. K. Komarala, *Appl. Phys. Lett.*, 2014, **105**, 033904.

116 S. K. Pathak, A. Abate, P. Ruckdeschel, B. Roose, K. C. Gödel, Y. Vaynzof, A. Santhala, S.-I. Watanabe, D. J. Hollman, N. Noel, A. Sepe, U. Wiesner, R. Friend, H. J. Snaith and U. Steiner, *Adv. Funct. Mater.*, 2014, **24**, 6046–6055.

117 W. Li, H. Dong, L. Wang, N. Li, X. Guo, J. Li and Y. Qiu, *J. Mater. Chem. A*, 2014, **2**, 13587–13592.

118 W. H. Nguyen, C. D. Bailie, E. L. Unger and M. D. McGehee, *J. Am. Chem. Soc.*, 2014, **136**, 10996–11001.

119 I. C. Smith, E. T. Hoke, D. Solis-Ibarra, M. D. McGehee and H. I. Karunadasa, *Angew. Chem.*, 2014, **126**, 11414–11417.